# Vibration control of a cantilever beam coupled with magnetic tri-stable nonlinear energy sink

Jundong Fu[a,b], Shui Wan[a*], Wenke Li[c], Jiwei Shen[a], Harikrishnan Venugopal[b], Mia Loccufier[b], and Kevin Dekemele[b]

[a]School of Transportation, Southeast University, Nanjing 211102, China

[b]Department of Electromechanical, Systems and Metal Engineering, Ghent University, Ghent 9052, Belgium

[c]College of Power and Energy Engineering, Harbin Engineering University, Harbin 150001, China

| | |
|---|---|
| Jundong Fu | E-mail: Jundong.Fu@UGent.be |
| Shui Wan | E-mail: 230198677@seu.edu.cn (Correspond author) |
| Wenke Li | E-mail: liwenke@hrbeu.edu.cn |
| Jiwei Shen | E-mail: 230198856@seu.edu.cn |
| Harikrishnan Venugopal | E-mail: Harikrishnan.Venugopal@UGent.be |
| Mia Loccufier | E-mail: Mia.Loccufier@UGent.be |
| Kevin Dekemele | E-mail: Kevin.Dekemele@UGent.be |

*Correspond author: Email address: 230198677@seu.edu.cn (S.Wan)

**Abstract:** In response to limitations in vibration suppression performance of traditional linear tuned mass damper (TMD) due to energy threshold constraints and narrow vibration bands, this study proposes a magnetic tri-stable NES (MTNES) formed by combining a linear spring and magnets. Compared to the conventional nonlinear energy sink (NES), the magnetic tri-stable NES (MTNES) incorporates magnetism to enhance the nonlinear stiffness. Firstly, the mechanism of the MTNES is introduced in this study, which reveals the existence of the three stable points in the system. Subsequently, the equations of motion of the coupled system with MTNES attached to the cantilever beam are derived, and the optimal parameter combination for MTNES is determined using a global optimization method. Furthermore, the influence of MTNES parameter variations on vibration suppression efficiency is studied through parameter analysis. Then, the restoring force of the MTNES is simplified into polynomial form, and the system response is analyzed using the harmonic balance method and Runge-Kutta method. Finally, experimental studies on the coupled system are conducted. The results indicate that MTNES can effectively suppress the resonance of the host structure within a wide frequency band, with the highest vibration suppression rate of up to 66% under strong modulated response. Additionally, the results of numerical calculations and theoretical analysis are in good agreement with that of the experiment.

**Keywords:** Magnetic tri-stable nonlinear energy sink; Cantilever beam; Vibration control; Harmonic balance method; Runge-Kutta method; Experimental validation.

## 1. Introduction

Vibration control is a critical area of study within engineering, particularly in relation to beam or rod structures. The tuned mass damper (TMD), functioning as a passive device to mitigate the host structures' vibrations, has found extensive application in vibration control within various engineering contexts [1, 2]. The TMD primarily mitigates the resonance frequency vibrations of the host structure. However, as the dynamic properties of the host structure change, the damping effectiveness of the TMD diminishes [3, 4]. A new device called the nonlinear energy sink (NES) has been introduced to enhance the broadband vibration absorption capabilities of damping devices. The nonlinearity in the NES is achieved through the incorporation of nonlinear stiffness, nonlinear damping, or inertial mass. Furthermore, it achieves excellent damping performance regardless of large amplitude transient vibration, harmonic excitation, or seismic load [5, 6].

In the past two decades, many types of NESs were proposed. Conventionally, the cubic NES (CNES) with cubic hardening nonlinear stiffness is the most widely studied NES. The dynamics of host system and NES are studied based on averaging method of complex variables and the multiple time-scale method, establishing the analytical solution of the strong nonlinear vibration of the CNES. The 1:1 internal resonance, super-harmonic, and sub-harmonic internal resonance behavior of its transient non-stationary response have been analyzed. Compared with the TMD, CNES has a broadband vibration absorption performance in terms of frequency [7-11]. However, one drawback is the limited energy dissipation range of the NES. To alleviate this issue, a bistable NES (BNES) can be used. Utilizing the strong nonlinear geometry of the springs, the BNES produces a continuous smooth alternation of nonlinear positive stiffness and negative stiffness during the response process resulting in two stable resting positions and one unstable one. Experimental and analytical results show that BNES has a wider energy dissipation range and an even wider vibration reduction frequency band than CNES [12-24]. The track NES is a novel energy-absorbing oscillator where the nonlinear restoring force is provided by using a nonlinear track for the oscillator motion.

Theoretical studies and experimental results indicate that as the stiffness of the host structure degrades, the TMD becomes detuned. Conversely, the track NES exhibits superior robustness in control performance compared to the TMD [25-29]. Vibro-impact NESs have high-frequency internal resonances behavior with the host structure, and dissipate energy through the impact of oscillators [30-35].

Other types of NESs include the gas-spring NESs [36-39], the rotary NESs [40, 41], NESs with nonlinear damping [42-44], multi-DOF NESs [45-47], and multi-stable NESs [48, 49], and scholars have conducted extensive research on the vibration reduction characteristics of these NESs through experimental, numerical, and theoretical analysis [50-54]. The use of permanent magnets to provide smooth nonlinear restoring forces in NESs has been increasingly investigated [22, 55-66]. Al. Shudeifat [52] proposed a new type of NES by introducing the NES based on asymmetric magnets. The magnetic NES significantly improved the shock mitigation performance over broadband energy input compared to the CNES. Chen et al. proposed a magnetic BNES for seismic control. By applying it to single-DOF and multi-DOF frame structures, the broadband and robustness of the magnetic NES were verified by using multiple seismic waves [22, 55]. Zeng et al. [56] introduced a method involving fixing a magnet in the center of a clamping pre-compressed beam and placing magnets on both sides of the fixed magnet to create a tri-stable NES (TNES). TNES can dissipate energy through inter-well chaotic oscillation between three stable points, to achieve the purpose of effectively suppressing vibration. Rezaei et al. [57-59] found that magnetic bi-stable NES (MBNES) and magnetic tri-stable NES (MTNES) can effectively suppress vibration in a wide frequency band, and their performance was better than that of linear vibration absorbers. Feudo et al. [60] applied the MBNES with adjustable linear stiffness to the research of vibration control of a three-story frame structure. The vibration of the host structure was significantly reduced under impact shock excitation, free vibration with initial displacement applied, and single-frequency excitation, indicating that MBNES can effectively control the vibration of the primary structure.

To summarize, the BNES and the TNES have the attractive features of a lower targeted energy transfer (TET) threshold, strongly modulated response (SMR), and more energy dissipation than the conventional NES. In addition, the magnet-spring mechanisms consisting of elastic springs and permanent magnets can achieve a wide variety of NES characteristic, such as multi-stable characteristics, and has the characteristics of adjustment of stiffness [61-63].

Hence, the use of multi-stable NESs to control vibration of the structures holds bright application prospects. Accordingly, this study creatively proposes a new NES with three stable points through coupling magnets with springs. Compared with existing TNES, the proposed TNES in this study has the characteristics of extreme simplicity (The system comprises solely an oscillator, guide rail, outer and inner magnets, and a spring.), allowing for great on-the-fly adjustability (Adjustable stable points are achieved in the MTNES by varying the size and arrangement of the inner and outer magnets along with the stiffness of the springs.), and strong nonlinearity (Nonlinear repulsion force generated by outer and inner magnets.). Additionally, a cantilever beam is chosen as the host structure while assessing the effectiveness of the new MTNES. Consequently, through a combination of theoretical analysis, numerical analysis and experimental verification, this study verifies that the proposed MTNES has a broadband vibration suppression effect and a high sensitivity to small vibrations at the endpoint of the cantilever beam.

This paper is organized as follows: In Section 2, the mechanical model and mechanism of the proposed MTNES are introduced. An optimization method for MTNES system parameters is proposed in section 3, and the effectiveness of the optimization method is verified by using parameter analysis under harmonic excitation. In Section 4, a comparative analysis of the response of the cantilever beam system coupled with MTNES is conducted using both the harmonic balance (HB) method and the Runge-Kutta (RK) method. In this case, the magnetic restoring force is simplified into polynomial form. In Section 5, the experiments on the dynamic analysis of the cantilever beam MTNES is carried out.

## 2. Proposed MTNES

According to [64], a previously proposed mechanism by the researchers obtained a magnetic-spring bi-stable NES (MBNES) through a careful selection of magnets and springs. Here, this mechanism is modified to allow for three stable points. Fig. 1 is the schematic diagram of the proposed MTNES with three different stable points by adding an additional set of symmetrical outer magnets to the MBNES design mentioned in [64]. The restoring force is generated by a combination of a spring and magnets that are symmetrically arranged on both sides of the oscillator. The restoring force between the inner and outer magnets is configured in repulsion. The magnets are identical and the length, height and thickness are *2a*, *2b* and *2c*, respectively. The distance between the outer surfaces of the inner and outer magnets is *d*. As shown in Fig.1(b), at the stable point 2, the distance between the two outer magnets is *e*. The distance between the center of the inner and outer magnets along the moving direction of the oscillator is *L*. The linear stiffness of the spring is $k_l$. As described in Fig. 1(a) and Fig. 1(c), the distance between the center of inner magnets of stable points 1 and 3 and the outer magnets in the moving direction is $L_m$. The magnetic charge model for the stiffness restoring force $F_\text{n}$ of the MTNES system is presented in [65, 66].

$$F_n = -k_l w - \frac{J^2}{2\pi\mu_0}\sum_{i=0}^{1}\sum_{j=0}^{1}\sum_{k=0}^{1}\sum_{l=0}^{1}\sum_{p=0}^{1}\sum_{q=0}^{1}(-1)^{i+j+k+l+p+q}[\Phi(w+L,d+c)+\Phi(w-L,d+c)]. \quad (1)$$

where $w$ is the displacement of the oscillator, $J$ is the polarization intensity of the magnets with a value of 1.34 T, $\mu_0$ is the vacuum permeability factor and generally considered as $4\pi\times10^{-7}$ H/m [65], and

$$\Phi(w\pm L,d+c) = \frac{Y_{kl}^2 - Z_{pq}^2}{2}\ln(S - X_{ij}) + X_{ij}Y_{kl}\ln(S - Y_{kl}) + Y_{kl}Z_{pq}\arctan(\frac{X_{ij}Y_{kl}}{SZ_{pq}}) + \frac{SX_{ij}}{2}. \quad (2)$$

$$\begin{aligned} X_{ij} &= (w\pm L) + (-1)^j a - (-1)^i a, \quad Y_{kl} = (-1)^l b - (-1)^k b, \\ Z_{pq} &= (d+c) + (-1)^q c - (-1)^p c, \quad S = \sqrt{X_{ij}^2 + Y_{kl}^2 + Z_{pq}^2}. \end{aligned} \quad (3)$$

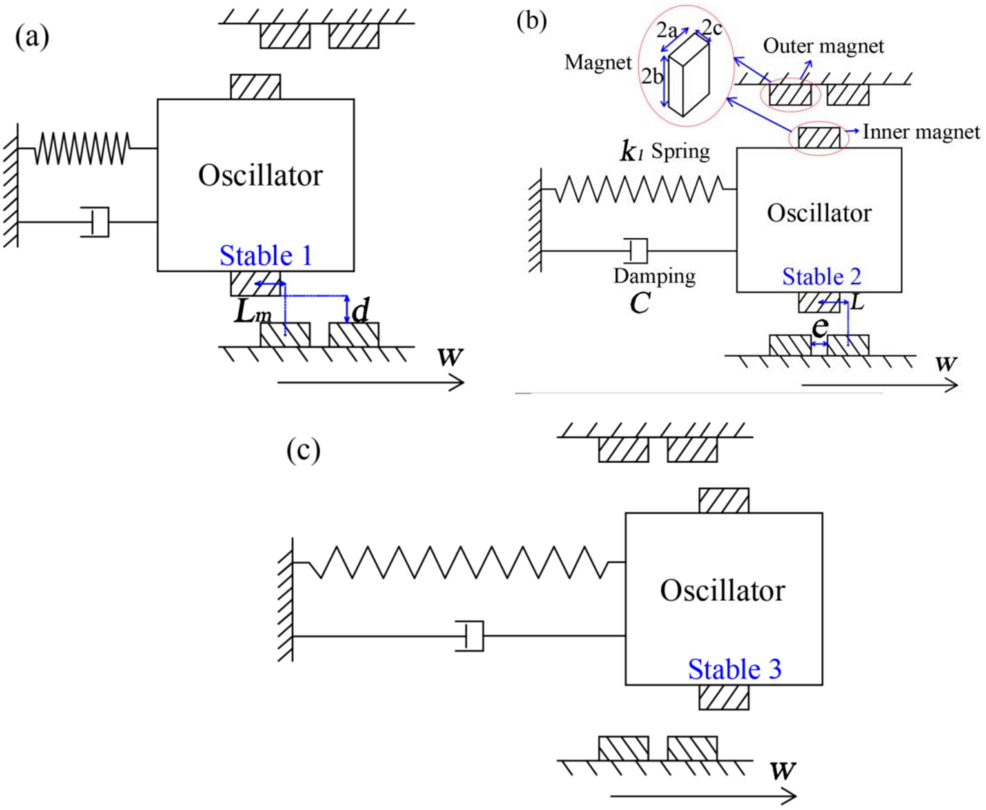

**Fig. 1** Schematic diagram of the three stable points of MTNES mechanism: (a) Stable point 1; (b) Stable point 2; (c) Stable point 3.

## 3. Cantilever beam with MTNES

### 3.1 Equations of motion

Fig. 2 depicts the schematic of the compound system. This system consists of a homogeneous Euler-Bernoulli cantilever beam and an MTNES. The governing equation of the system is given by [62, 63, 67-70],

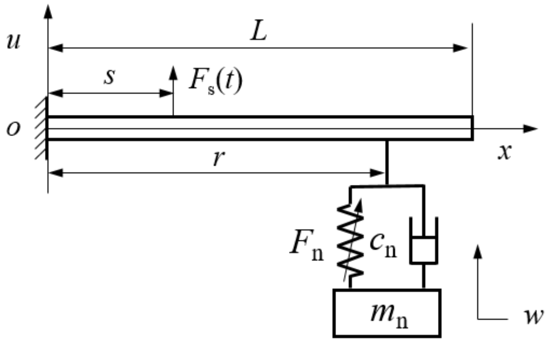

**Fig. 2** A cantilever beam coupled to an MTNES.

$$
\begin{aligned}
&Mu_{tt}(x,t)+EIu_{xxxx}(x,t)+Cu_{t}(x,t)+\{F_n+c_n[\dot{w}(t)-u_t(r,t)]\}\delta(x-r)\\
&=F\cos(\Omega t)\delta(x-s),\\
&m_n\ddot{w}(t)+c_n[\dot{w}(t)-u_t(r,t)]+F_n=0.
\end{aligned}
\tag{4}
$$

Where the subscripts $t$ and $x$ represent the partial differentiation with respect to time and displacement, respectively. $M$ is the mass density per meter, $E$ is the elastic modulus of the steel, $I$ is the moment of inertia, and $C$ is the equivalent viscous damping of the host structure. The displacement of the host structure is $u(x,t)$. $w(\mathrm{t})$, $\dot{w}(\mathrm{t})$ and $\ddot{w}(\mathrm{t})$ represent the displacement, velocity, and acceleration of the oscillator, respectively. $m_\mathrm{n}$ is the mass of the oscillator, $c_\mathrm{n}$ is the damping coefficient in the MTNES, and $F_\mathrm{n}$ is the nonlinear restoring force in the MTNES. $\delta$ is the Dirac function. The $n^{\mathrm{th}}$ vibration mode $\phi_n$ and the natural frequency $\omega_\mathrm{n}$ of the cantilever beam are given by,

$$\begin{aligned}\phi_n(x) = A_n\{&[\sin(\beta_n L)+\sinh(\beta_n L)][\sin(\beta_n x)-\sinh(\beta_n x)]\\ &+[\cos(\beta_n L)+\cosh(\beta_n L)][\cos(\beta_n x)-\cosh(\beta_n x)]\}.\end{aligned} \tag{5}$$

$$\omega_n = \beta_n^2\sqrt{\frac{EI}{M}}. \tag{6}$$

where $A_n$ is the amplitude of the mode and $\beta_n$ is calculated by,

$$A_n = \{\int_0^L M[\frac{\phi_n(x)}{A_n}]^2 dx\}^{-\frac{1}{2}}. \tag{7}$$

$$1+\cos(\beta_n L)\cosh(\beta_n L)=0. \tag{8}$$

The geometric displacement coordinates of the cantilever beam are converted into generalized coordinates, represented by the mode shape amplitude, through the utilization of the Galerkin method. The expression is given by,

$$u(x,t)=\sum_{h=1}^{\infty} q_h(t)\phi_h(x) \qquad h\in \mathrm{Z}^+. \tag{9}$$

In this compound system, only the first bending mode of the cantilever beam is modeled, that is $h = 1$, so the Eq. (4) can be written as,

$$\begin{aligned}&b_{f1}\ddot{q}_1(t)+2\xi_1\omega_1 b_{f1}\dot{q}_1(t)+b_{s1}q_1(t)+\{c_n[\dot{q}_1(t)\phi_1(r)-\dot{w}(t)]-F_n\}\phi_1(r)\\ &=F\cos(\Omega t)\phi_1(s),\\ &m_n\ddot{w}(t)+c_n[\dot{w}(t)-\dot{q}_1(t)\phi_1(r)]+F_n=0.\end{aligned} \tag{10}$$

Where

$$b_{f1}=M\int_0^L \phi_1^2(x)dx, \qquad b_{s1}=EI\int_0^L \frac{d^4\phi_1(x)}{dx^4}\phi_1(x)dx. \tag{11}$$

The parameters of the cantilever beam that also will be used in the experiments are given in Table 1. The excitation point of the external load is at 0.2L away from the fixed point of the cantilever beam, specifically, s = 0.297 m. The MTNES is situated at the end point of the cantilever beam, with r = 1.486 m.

**Table 1** The parameters of the cantilever beam

| $L$ | $D$ (Width) | $T$ (Thickness) | $\rho$ (Density) |
|---|---|---|---|
| 1.486 m | 0.076 m | 0.0122 m | $7.85\times10^3$ kg/m$^3$ |
| $M$ | $I$ | $E$ | $\xi_n$ (Equivalent damping coefficient) |
| 7.278 kg/m | $1.15\times10^{-8}$ m$^4$ | 206 GPa | 0.75% [72] |
| $b_{s1}$ | $b_{f1}$ | $\Phi_1(L)$ | $\Phi_1(s)$ |
| $1.66\times10^4$ | 20.07 | 2.724 | 0.174 |

According to the parameters listed in Table 1, the natural frequency $\omega_1$ is 28.7 rad/s (4.57 Hz). In this model, the harmonic load is used as the external load, that $F_s(t) = F\cdot\cos(\Omega\cdot t)$. $F$ and $\Omega$ are the amplitude and frequency of the harmonic load. The total mass of the cantilever beam is $m = 10.816$ kg. As suggested in [27, 55, 71], the ratio of the mass of the oscillator $m_\mathrm{n}$ to the mass of the host structure $\gamma$ is set as 0.05, i.e. $m_\mathrm{n} = 0.54$ kg . As recommended in [72], the equivalent damping coefficient $\xi_1$ is 0.75%. The damping coefficient is $c_\mathrm{n}$, and the nonlinear restoring force is $F_\mathrm{n}$.

## 3.2 Optimization of MTNES

Determining optimal parameters for the MTNES is crucial to achieving the most effective vibration reduction. Furthermore, it is also a crucial factor in ensuring that MTNES exhibits three stable points. The impact load is used as an external excitation load for parameter optimization. An initial velocity is applied at the end point of the cantilever beam and set as $0.2\sqrt{2}$ m/s in the first mode, allowing the oscillator within MTNES to undergo a steady-state transition during the initial stages of vibration control [26, 55, 64]. The optimizing objective function is given by,

$$I = \max\frac{1}{2}\left(\frac{E_{MTNES}}{E_{ini}} + \frac{D_{RMS,U} - D_{RMS,C}}{D_{RMS,U}}\right). \tag{12}$$

Where $E_\mathrm{MTNES}$ is the total energy dissipated by MTNES. $E_\mathrm{ini}$ is the initial input energy in the host structure. $D_\mathrm{RMS,U}$ and $D_\mathrm{RMS,C}$ are the root mean square (RMS) displacement of the endpoint of the uncontrolled and controlled host structure. The expression of $E_\mathrm{MTNES}/E_\mathrm{ini}$ and $(D_\mathrm{RMS,U}-D_\mathrm{RMS,C})/D_\mathrm{RMS,U}$ are given by,

$$\frac{E_{MTNES}}{E_{ini}} = \frac{c_n\sum_{i=1}^{n}(\dot{w}(i)-\dot{u}(i))^2 dt}{\frac{1}{2}\omega_1^2\int_0^L M[\dot{u}(x,t)]^2 dx},\quad \frac{D_{RMS,U} - D_{RMS,C}}{D_{RMS,U}} = \frac{\sqrt{\frac{1}{n}\sum_{i=1}^{n}U_i^2} - \sqrt{\frac{1}{n}\sum_{i=1}^{n}u_i^2}}{\sqrt{\frac{1}{n}\sum_{i=1}^{n}U_i^2}}. \tag{13}$$

The more the objective $I$ approaches 1, the better the control performance of the

NES. The deflection of the cantilever beam $u(x,t)$ is assumed to be the product of the first mode shape $\phi_1$ and a general coordinate $q(t)$, as shown in

$$\begin{aligned} u(x,t) = \phi_1(x)q_1(t) = A_1\{&[\sin(\beta_1 L)+\sinh(\beta_1 L)][\sin(\beta_1 x)-\sinh(\beta_1 x)] \\ &+[\cos(\beta_1 L)+\cosh(\beta_1 L)][\cos(\beta_1 x)-\cosh(\beta_1 x)]\}q_1(t). \end{aligned} \tag{14}$$

A global optimization method is used to obtain the parameters of the MTNES. The total time of the simulation is 15 seconds for each parameter combination. According to [64, 73, 74], the design parameters $k_{\mathrm{TMD}}$ (the optimal spring stiffness) and $c_{\mathrm{TMD}}$ (the optimal damping coefficient) of TMD should be calculated first, and then use these two parameters as the reference to determine the optimization range of linear spring stiffness ($k_l$) and damping coefficient ($c_l$) in MTNES. These parameters are calculated by

$$\begin{cases} f_{TMD} = \dfrac{1}{1+\gamma}(\sqrt{\dfrac{2-\gamma}{2}}) & \xi_{TMD} = \sqrt{\dfrac{3\gamma}{8(1+\gamma)}}(\sqrt{\dfrac{2}{2-\gamma}}) \\ k_{TMD} = f_{TMD}^2\omega_1^2 m_n & c_{TMD} = 2\xi_{TMD} f_{TMD}\omega_1 \end{cases} \tag{15}$$

Where $k_{\mathrm{TMD}}$ and $c_{\mathrm{TMD}}$ are 393 N/m and 7.3 N/(m/s). Taking into account that the parameters of MTNES devices should be easily obtained, the optimization scope of magnets' size, the optimization step are listed in Table 2. Simultaneously, in order to make the parameter optimization scope of $k_l$ and $c_l$ contain $k_{\mathrm{TMD}}$ and $c_{\mathrm{TMD}}$, the optimization scope of $k_l$ is set from 150 N/m to 450 N/m, with step size 10 N/m and the scope of $c_l$ is set from 2 N/(m/s) to 20 N/(m/s), with step size 1 N/(m/s) [55,64]. Before calculating each set of parameters by using the 4th order Runge-Kutta method, it is initially confirmed that the nonlinear restoring force curve of the MTNES intersects the X-axis at five points. For each step, the objective function $I$ is computed, and the $I_{\max}$ is 0.768.

**Table 2** Optimization parameters of MTNES

| Parameter | Optimization scope | Optimization step size | Optimal value | $I_{\max}$ |
|---|---|---|---|---|
| $2a$(mm) | 10-30 | 2 | 20 | 0.768 |
| $2b$(mm) | 5-15 | 1 | 10 | |
| $2c$(mm) | 1-5 | 1 | 4 | |
| $d$(mm) | 1-10 | 1 | 6 | |
| $e$(mm) | 0-5 | 1 | 0 | |
| $k_l$(N/m) | 150-450 | 10 | 210 | |
| $c_l$(N/(m/s)) | 2-20 | 1 | 8 | |

Fig. 3 displays the restoring force and potential energy of the optimized MTNES system. It is obvious that the restoring force curve has 5 intersection points with the x-axis and the potential energy curve has three potential sinks which correspond to three stable points. Fig. 4 shows the displacement attenuation of the beam's endpoint with initial velocity ( $0.2\sqrt{2}$ m/s) under controlled and uncontrolled conditions. It is apparent that the MTNES can quickly absorb and dissipate the vibration energy in the host structure.

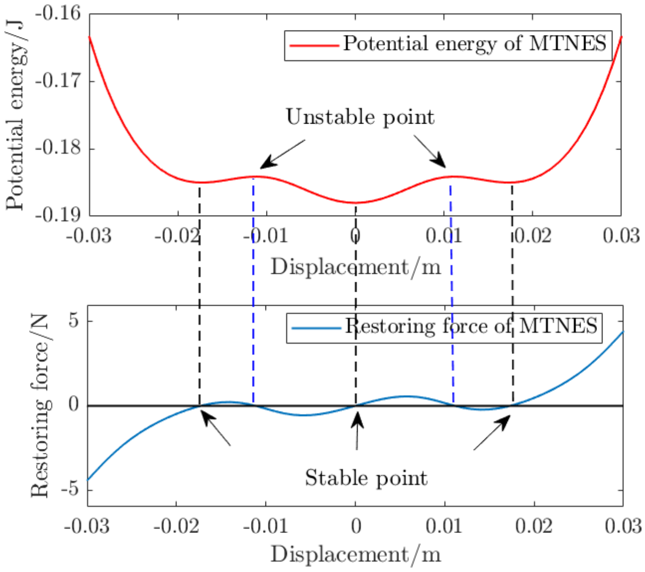

**Fig. 3** Restoring force curve and potential energy curve of the optimized MTNES.

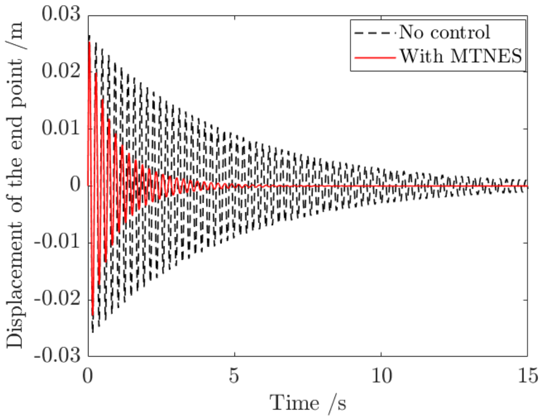

**Fig. 4** Displacement of the endpoint of the cantilever beam with and without MTNES.

## 3.3 Parameter sensitivity analysis under harmonic force

To verify the applicability of the optimization method (Eq.12) in the previous section also provides excellent performance under harmonic force, it is necessary to analyze the parameters that affect the vibration response of the system. The efficacy of energy dissipation of the MTNES is significantly influenced by its position on the cantilever beam, the location and the magnitude of the external load, spring stiffness, viscous damping, and the mass ratio of the oscillator in the MTNES. The energy dissipated in the MTNES is derived from the governing expression and described as,

$$E_T = \frac{\int_0^{T_{\mathrm{tot}}} c_n \left\{\left[\dot{w}(t) - \dot{q}_1(t)\phi_1(r)\right]\right\}^2 dt}{\int_0^{T_{tot}} F_s(t)\dot{q}_1(t)\phi_1(s)dt}. \tag{16}$$

Where $T_{\mathrm{tot}}$ is the total time of harmonic loading excitation and set as 15 seconds. The closer for the energy dissipation ratio $E_{\mathrm{T}}$ is to 1, the better dynamic control performance of MTNES. Based on the calculation results in Fig. 5, the impact of harmonic loads cause the coupled structure to exhibit a transient response in the initial stage or strong modulated response (SMR) which will discuss in detail later, leading to a non-smooth phenomenon. When $F$ is 150 N, Ω is 4.5 Hz, and $s$ is 0.297 m, as MTNES moves closer to the endpoint of the beam, it becomes more efficient at absorbing and dissipating the energy from the host structure. As depicted in Fig. 5(a), the maximum energy dissipation ratio is 88.8%. Therefore, in the subsequent parameter analysis, MTNES is positioned at the endpoint of the cantilever beam.

Fig. 5(b) illustrates the variation in the energy consumption ratio concerning the magnitude of the external load. The MTNES exhibits effective vibration reduction and energy dissipation within the range from 50 N to 200 N of the external loads. It shows a plateau near 0.88, indicating a saturation in performance. As depicted in Fig. 5(c), when $F$ is 150N, with $s$ ranging from 0.1486 m to 1.486 m (0.1$L$ to $L$) away from the fixed end of the cantilever beam, the energy dissipated by MTNES in relation to the input energy initially increases and then decreases. Particularly within the range of 0.1486 m to 0.4458 m (0.1$L$ to 0.3$L$), the MTNES exhibits the capacity to absorb and dissipate over 75% of the input energy. The peak value occurs at the position 0.372 m (0.25$L$) away from the fixed end. The results depicted in Fig. 5(d) indicate that MTNES achieves optimal energy dissipation capability when the mass ratio approaches 0.05. However, when the mass ratio is over 0.05, the energy dissipation effectiveness of the MTNES does not notably increase and instead exhibits a slight downward trend.

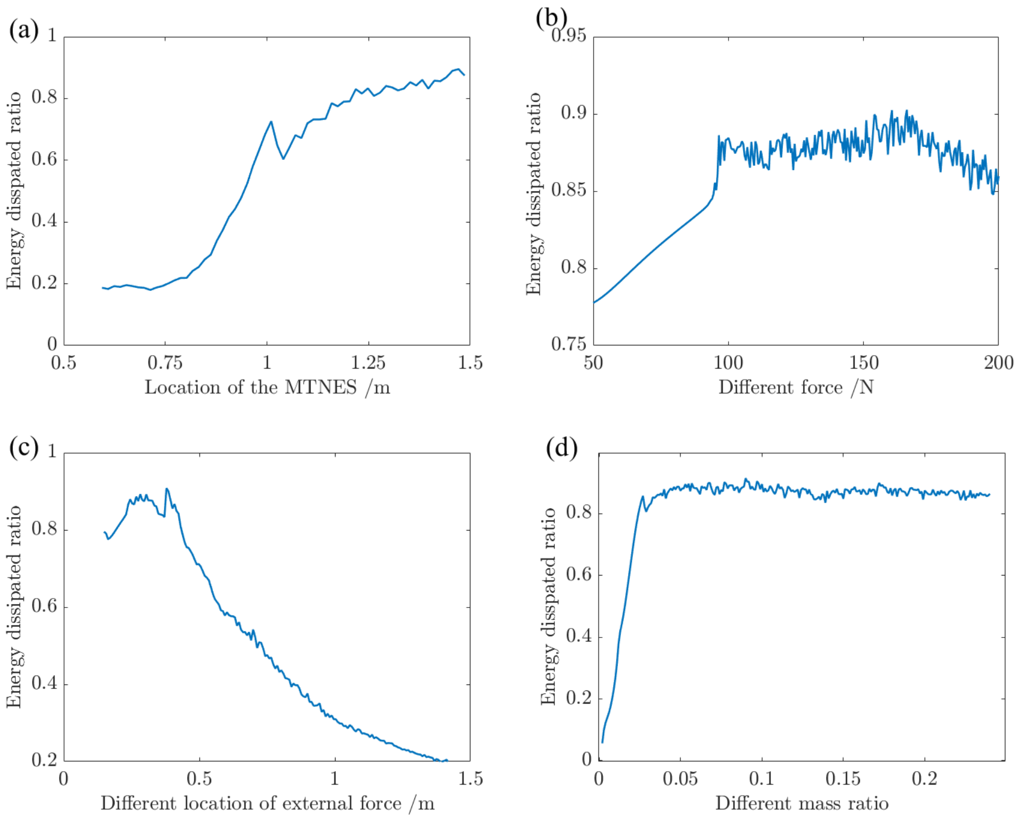

**Fig.5** Energy dissipated ratio: (a) Different location of the MTNES; (b) Different amplitude of the external load; (c) Different location of the external load; (d) Different mass ratio.

Fig. 6 illustrates the linear stiffness and linear damping in MTNES effect on the energy dissipated ratio. During the parameter analysis of the MTNES, with s=0.297 m, $F$ is 150 N, $r$=1.486 m, and $m_n$=0.54 kg. Note that when keeping the magnets in the MTNES constant and the spring stiffness is between 90 N/m and 220 N/m, there are three steady-state points in the MTNES. When the linear stiffness $k_l$ is 210 N/m and the damping coefficient is 9 N·s/m, the MTNES shows the best energy dissipation performance of 0.891. The obtained parameters are nearly identical to those optimized with impact load as the external load.

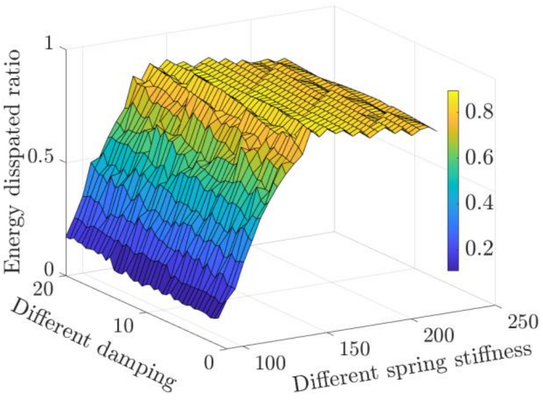

**Fig.6** The impact of the combination of linear spring stiffness and damping in MTNES on the energy dissipated ratio.

# 4. Vibration reduction analysis

## 4.1 Simplification of restoring force

The complex restoring force described in Eq. (1) makes further analysis difficult. Therefore, the nonlinear force expression (visualized in Fig. 3) is approximated here by a polynomial series, proven to be accurate for other complex restoring forces [56, 75]. The least squares method is used to perform the polynomial approximation of an interval, and the expression is obtained as,

$$\begin{aligned} F_n &= k_1 x + k_3 x^3 + k_5 x^5 + k_7 x^7 + k_9 x^9 \qquad\qquad x \in [-0.032, 0.032]\ \mathrm{m} \\ &= 129.18x - 1.52\times10^6 x^3 + 5.32\times10^9 x^5 - 6.67\times10^{12} x^7 + 2.97\times10^{15} x^9 . \end{aligned} \tag{17}$$

Fig. 7 compares the polynomial restoring force curve and the magnetic restoring force curve, showing a good agreement within the fitted range of ± 0.032 m.

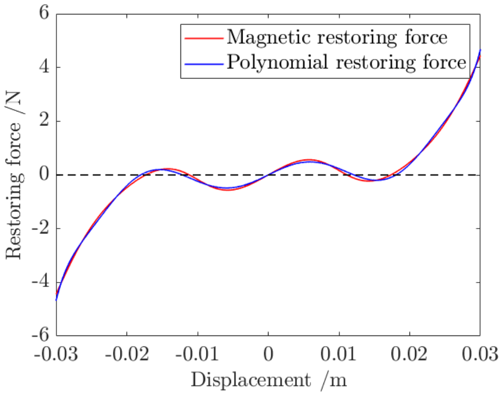

**Fig.7** Comparison between magnetic restoring force and polynomial restoring force.

A numerical simulation is done to compare the fit dynamically. The harmonic external load $F_s(t)=60\cdot\cos(2\pi\cdot4.5\cdot t)$ is used to numerically analyze the response of the coupled system using magnetic restoring force and polynomial restoring force. The endpoint's displacement response and the oscillator's relative displacement response calculated using the two nonlinear restoring force models shown in Fig. 8(a) and Fig. 8(b) are almost consistent. Although there is a slight deviation in the oscillator's response during the initial stage, primarily due to its oscillation near the unstable point. However, the steady-state response is consistent. Thus, for harmonic loads under steady state, the polynomial fitting restoring force model can replace the magnetic restoring force model to allow further analytical investigations.

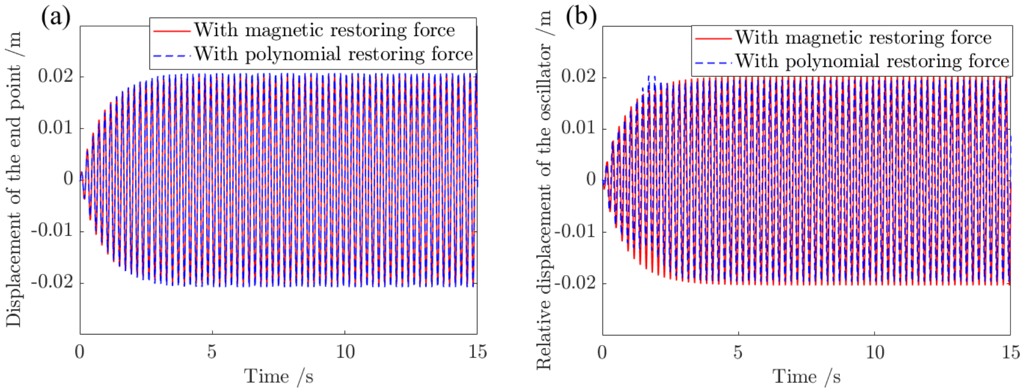

**Fig.8** Comparison of system response between using polynomial restoring force and magnetic restoring force: (a) Displacement of the endpoint; (b) Relative displacement of the oscillator.

## 4.2 Harmonic balancing method

The vibration control performance of MTNES will be analyzed using the harmonic balance (HB) method [76-81], where a harmonic solution is proposed for the displacement. The Eq.(10) which contains the restoring force of the MTNES expressed in polynomial form is given by,

$$\begin{aligned}&\frac{b_{f1}}{\phi_1(L)}\ddot{u}+\frac{2\xi_1\omega_1 b_{f1}}{\phi_1(L)}\dot{u}+\frac{b_{s1}}{\phi_1(L)}u+m_n\phi_1(L)\ddot{w}=F\cos(\Omega t)\phi_1(s),\\&m_n\ddot{w}+c_n(\dot{w}-\dot{u})+\sum_{\gamma=1}^{9}k_\gamma(w-u)^{\gamma}=0 \qquad (\gamma=1,3,5,7,9).\end{aligned} \tag{18}$$

Only the first mode of the cantilever beam is taken into consideration. The relative displacement between the oscillator of MTNES at the endpoint of the cantilever beam is $z$ ($z=w-u$). After some manipulation and introducing dimensionless time ($\tau=\omega_1 t$), Eq. (18) becomes,

$$\begin{aligned}&\ddot{u}+2\xi_1\dot{u}+u+\varepsilon(\ddot{z}+\ddot{u})=\varepsilon\overline{F}\cos(\overline{\Omega}\tau),\\&\varepsilon(\ddot{z}+\ddot{u})+\varepsilon\xi_n\dot{z}+\varepsilon\sum_{\gamma=1}^{9}\overline{k_\gamma}z^{\gamma}=0 \quad (\gamma=1,3,5,7,9).\end{aligned} \tag{19}$$

Where $\varepsilon=\dfrac{m_n\phi_1^2(L)}{b_{f1}}$, $\overline{F}=\dfrac{F\phi_1(s)}{\omega_1^2 m_n\phi_1(L)}$, $\overline{\Omega}=\dfrac{\Omega}{\omega_1}$, $\xi_n=\dfrac{c_n}{m_n\omega_1}$, $\overline{k_\gamma}=\dfrac{k_\gamma}{m_n\omega_1^2}$.

Then, the harmonic balance method is used to analyze the system under the action of harmonic excitation of a single frequency $\overline{\Omega}$. The complex Manevitch variables $A$ and $B$ are introduced [77, 78],

$$2A(\tau)e^{i\overline{\Omega}\tau}=x-i\frac{\dot{x}}{\overline{\Omega}}, \qquad 2B(\tau)e^{i\overline{\Omega}\tau}=z-i\frac{\dot{z}}{\overline{\Omega}}. \tag{20}$$

The original variables $u$ and $z$ in Eq. (19) can then be substituted by,

$$\begin{aligned} &u(\tau)=A(\tau)e^{i\overline{\Omega}\tau}+A^*(\tau)e^{-i\overline{\Omega}\tau}, && z(\tau)=B(\tau)e^{i\overline{\Omega}\tau}+B^*(\tau)e^{-i\overline{\Omega}\tau}. \\ &\dot{u}(\tau)=i\overline{\Omega}[A(\tau)e^{i\overline{\Omega}\tau}-A^*(\tau)e^{-i\overline{\Omega}\tau}], && \dot{z}(\tau)=i\overline{\Omega}[B(\tau)e^{i\overline{\Omega}\tau}-B^*(\tau)e^{-i\overline{\Omega}\tau}]. \\ &\ddot{u}(\tau)+\overline{\Omega}^2u(\tau)=i2\overline{\Omega}\dot{A}(\tau)e^{i\overline{\Omega}\tau}, && \ddot{z}(\tau)+\overline{\Omega}^2z(\tau)=i2\overline{\Omega}\dot{B}(\tau)e^{i\overline{\Omega}\tau}. \end{aligned} \tag{21}$$

Substituting (20) into (18) and only keeping the terms with $e^{i\overline{\Omega}\tau}$ yields,

$$\begin{aligned} &i2\overline{\Omega}\dot{A}+(1-\overline{\Omega}^2)A+i2\xi_1\overline{\Omega}A+\varepsilon[i2\overline{\Omega}\dot{B}+i2\overline{\Omega}\dot{A}-\overline{\Omega}^2A-\overline{\Omega}^2B]=\frac{1}{2}\varepsilon\overline{F}, \\ &i2\overline{\Omega}(\dot{A}+\dot{B})-\overline{\Omega}^2(A+B)+\xi_n i\overline{\Omega}B+\sum_{\gamma=1}^{9}\overline{k_\gamma}C_\gamma^{\frac{\gamma+1}{2}}B^{\frac{\gamma+1}{2}}B^{*\frac{\gamma-1}{2}}=0 \quad (\gamma=1,3,5,7,9). \end{aligned} \tag{22}$$

In the situation of steady state response, where $A'=B'=0$, Eq.(22) can be reduced to,

$$\begin{aligned} &(1-\overline{\Omega}^2)A+i2\xi_1\overline{\Omega}A-\varepsilon(\overline{\Omega}^2A+\overline{\Omega}^2B)=\frac{1}{2}\varepsilon\overline{F}, \\ &-\overline{\Omega}^2(A+B)+\xi_n i\overline{\Omega}B+\sum_{\gamma=1}^{9}\overline{k_\gamma}C_\gamma^{\frac{\gamma+1}{2}}B^{\frac{\gamma+1}{2}}B^{*\frac{\gamma-1}{2}}=0 \quad (\gamma=1,3,5,7,9). \end{aligned} \tag{23}$$

Additionally, the complex variables $A$ and $B$ can be written in polar form as $A=ae^{i\alpha}/2$ and $B=be^{i\beta}/2$. The second equation of Eq. (23) can be manipulated into a situation where the module of $A$ is equal to the module of $B$. Let $Z_a=a^2$ and $Z_b=b^2$, the first slow invariant manifold (SIM) between $Z_a$ and $Z_b$ can be obtained as,

$$\begin{aligned} &X^2Z_a=Z_b[X\xi_n^2+(X-\overline{K}(Z_b))^2], \\ &\overline{K}(Z_b)=\overline{k_1}+\frac{3}{4}\overline{k_3}Z_b+\frac{10}{16}\overline{k_5}Z_b^2+\frac{35}{64}\overline{k_7}Z_b^3+\frac{126}{256}\overline{k_9}Z_b^4. \end{aligned} \tag{24}$$

Simultaneously, via combining the two equations in Eq. (23), the SIM between $Z_b$ and $\overline{F}$ can also be obtained as,

$$[X(\sigma+\xi\xi_n)+(X-\sigma)\overline{K}(Z_b)]^2Z_b+[\xi(\overline{K}(Z_b)-X)+\xi_n(\sigma-X)]^2XZ_b=(X\overline{F})^2. \tag{25}$$

Where $X=\overline{\Omega}^2$, $\sigma=\dfrac{1-X}{\varepsilon}$, $\xi=\dfrac{2\xi_1}{\varepsilon}$.

The stability of Eq. (24) is computed in Appendix A and the stability of Eq. (25) is shown in Appendix B. If the excitation amplitude $\overline{F}$ of the external load is chose, the relationship between the excitation frequency $\overline{\Omega}$ and $Z_b$ can be determined via Eq. (25). Then the relationship between $Z_a$ and $\overline{\Omega}$ is obtained from Eq. (24), obtaining a frequency response. Next, A comparison between the frequency response obtained from HB, the simulation results by using the RK method from Eq. (18)

## 4.3 Comparison between RK and HB method

Fig. 9 illustrates the response of the system in detail. The thicker lines in Fig. 9(a) show the response amplitude of the controlled structure obtained from Eq.(24) and Eq.(25) via the HB method and the thinner lines are the response amplitude of the uncontrolled structure. The solid lines and the dashed lines correspond to stable solutions and unstable solutions, respectively. $\sqrt{Z_a^+}$ (the dashed black line above) and $\sqrt{Z_a^-}$ (the dashed black line below) correspond with the local maximum amplitude and minimum amplitude of the SIM with different $\overline{\Omega}$. Compared with the response of the uncontrolled host structure in the frequency domain, MTNES can effectively suppress the response amplitude of the host structure in a wide frequency band (from $\overline{\Omega} = 0.88$ to $\overline{\Omega} = 1.12$). Additionally, the MTNES will cause the response of the cantilever beam to distort and saturate near the resonance frequency. However, when the amplitude of the external load gets larger and $\overline{\Omega}$ is between 0.75 and 0.9, a bifurcation leads to the existence of an isolated response which is an undesirable response since it exhibits almost the same amplitude compared to the response without the MTNES.

Fig. 9(b) features two slow invariant manifolds (SIM) calculated by Eq.(24) for $\overline{\Omega} = 1$ and $\overline{\Omega} = 0.82$ when the amplitude of the external force is 180 N. The SIM shows the shape of 'S' and has the characteristics of the local maximum point and the local minimum point. In particular, as exhibited in Fig.9(c) where the red line is the upper envelope of the response in the time domain, when $\overline{\Omega} = 1$, due to the suppression effect of MTNES on the vibration of the host structure, a situation called a strong modulation response (SMR) occurs, where the MTNES and the host structure's vibration amplitude is modulated and energy is continuously exchanged between the MTNES and the cantilever beam. This occurs around the resonance frequency where the frequency response is unstable.

The blue colored line in Fig. 9(b) represents the envelope of the response of the host structure and oscillator, obtained from the simulation of Fig. 9(c). The mechanism driving the SMR is the SIM, the right branch of the SIM descended, resulting in a reduction in the amplitude of the host structure. Once the minimum value of SIM is attained, the dynamics transition to the left branch. Then, the dynamics ascend along the left branch, upon reaching the maximum value of SIM, the dynamics return to the right branch, thus completing the reciprocating motion cycle, clarifying the periodic modulation of the vibration amplitude.

The time domain responses shown in Fig. 9(d) and Fig. 9(e) correspond to the red point ($\overline{\Omega} = 1$) and the green point ($\overline{\Omega} = 0.82$) in the SIM (Fig.9(b)), respectively. The red point in the left branch (without initial velocity) of the SIM corresponds to the lower point in the left branch in Fig. 9(a) and has a lower amplitude response compared with the green point ($\dot{x}(0) = 2\sqrt{2}$) in the right branch corresponding to the upper point in the left branch in Fig. 9(a). This implies that in a coupled system, even if the frequency of the external excitation load is not near the resonance frequency of the host structure, under specific initial conditions, the response of the host structure and the oscillator may transition to the isolated branch, and its response may be higher than that of uncontrolled structures.

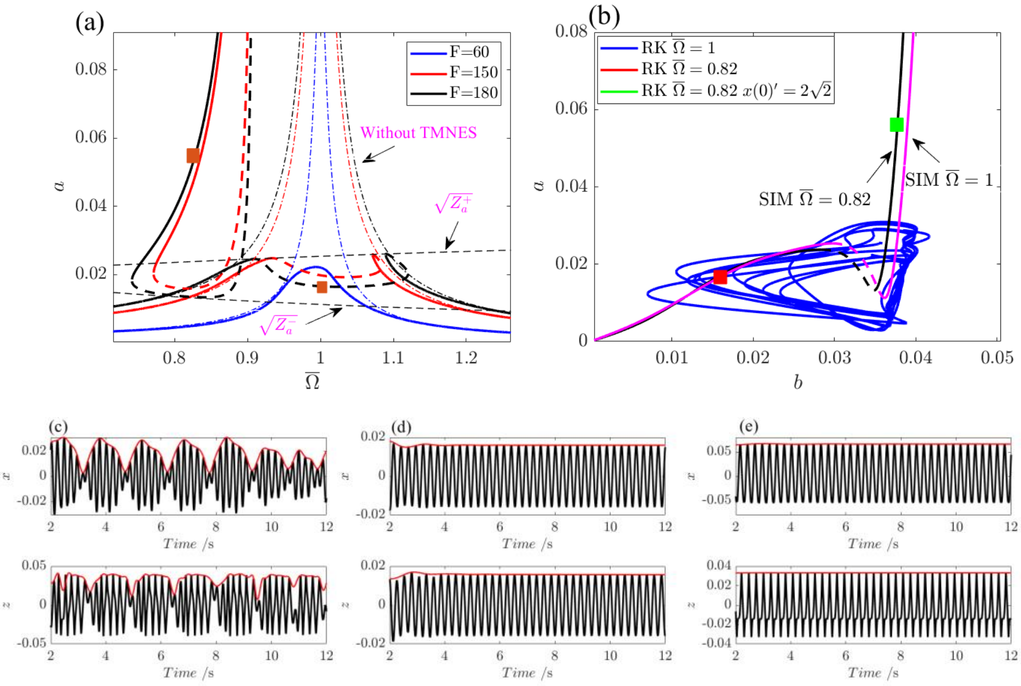

**Fig. 9** Analysis of the compound system: (a) HB analysis with different *F*; (b) SIMs for two different frequencies; (c) system response when $\overline{\Omega}$ =1 (RK method); (d) system response when $\overline{\Omega}$ =0.82 (RK method); and (e) system response when $\overline{\Omega}$ =0.82, with $\dot{x}(0) = 2\sqrt{2}$ (RK method).

Fig. 10(a) compares the typical behavior comparing the results of the HB method with the results obtained through the RK method. Specifically, during periods of steady-state response in the host structure, the results by using the RK method correspond closely to those by using the HB method. Furthermore, in instances of SMR, the maximum and minimum response amplitude computed by the RK method correspond to the local maximum (the dashed line above) and local minimum (the dashed line below) values of SIM, respectively. The RMS values derived from the RK method also reflect the results of the HB method. Upon increasing the external load amplitude to 180 N, as depicted in Fig. 10(b), compared to Fig.10(a), the isolated response touches the main branch of HB. Consequently, for several frequencies $\overline{\Omega}$, the response calculated by the RK method transitions into an isolated response, resulting in an undesirable high-amplitude response in the host structure.

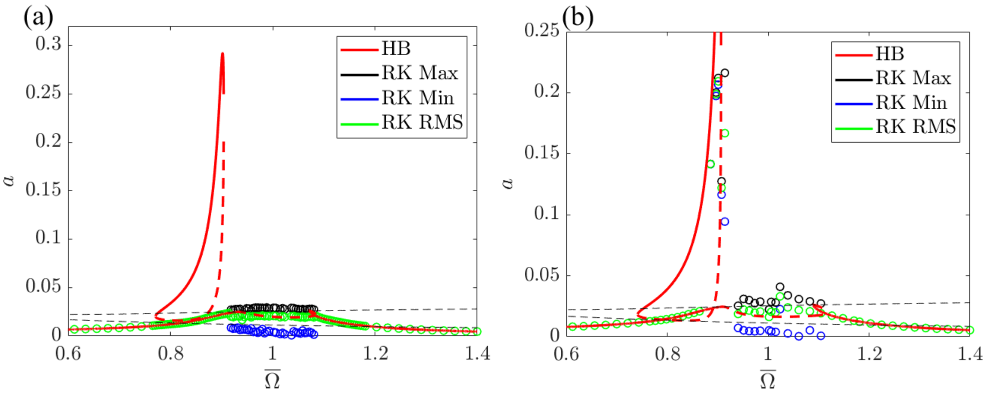

**Fig. 10** Frequency response comparison between the HB method and the RK method: (a) $F$=150 N; (b) $F$=180 N.

## 5. Experimental validation

### 5.1 Experimental setup

The experimental setup is depicted in Fig. 11. The parameters of the cantilever beam and the MTNES are the same as mentioned in Table 1 and Table 2. The position of the external load (0.2$L$ away from the fixed point) and the MTNES (at the end of the cantilever beam) are the same as those explained in the previous sections. The damping force is generated because of the relative motion between the oscillator in the MTNES and the rail passing through it. The oscillator is made of copper and other parts are made of aluminum alloy to avoid affecting the nonlinear forces provided by the magnets. To apply the force, firstly, the harmonic signal is generated by the signal generator, and then amplified by the power amplifier, and is finally transmitted to the shaker to excite the cantilever beam. The displacements of the excitation point and the endpoint of the cantilever beam are obtained through two laser displacement sensors. The displacement of the oscillator is obtained by collecting its acceleration during motion and integrating it twice. The load of the excitation point is obtained through a load sensor. The data sampling frequency is 1000 Hz.

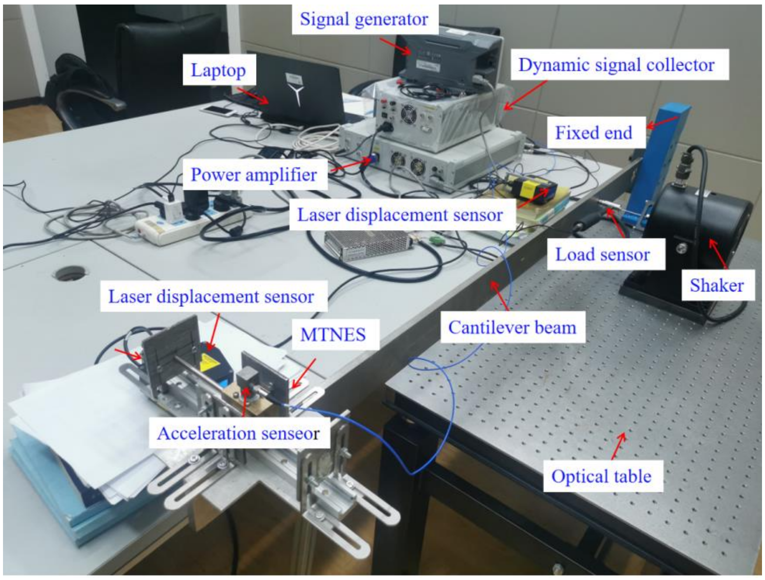

**Fig. 11** Experimental setup.

Fig. 12 is the diagram of the locations of the three steady-state points in the MTNES, which is consistent with what is shown in Fig. 1.

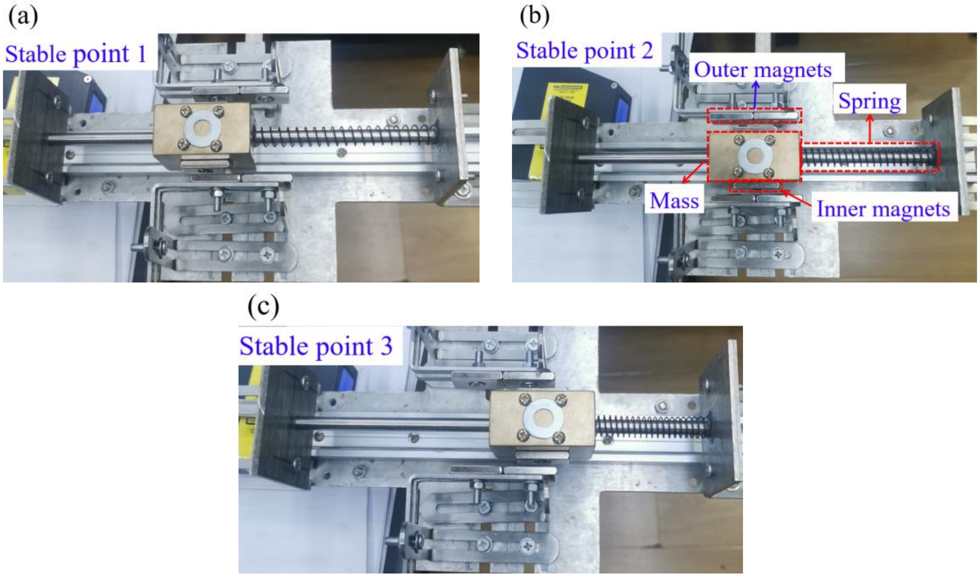

**Fig. 12** Stable points in MTNES: (a) Stable point 1; (b) Stable point 2; (c) Stable point 3.

## 5.2 System identification

The identification of the system includes the dynamic parameters of the cantilever beam and the MTNES. The cantilever beam is swept with a harmonic load excitation with frequency range from 0.5 Hz to 10 Hz, and the displacement response of the endpoint of the cantilever beam is shown in Fig. 13. By using the fast Fourier transform (FFT) method, the first natural frequency of the cantilever beam is 4.517 Hz, which is almost consistent with the theoretical calculation of 4.57 Hz. Simultaneously, the damping ratio of the cantilever beam obtained by applying the resonance amplification method is 0.763%, which is almost the same as the 0.75% recommended by [72].

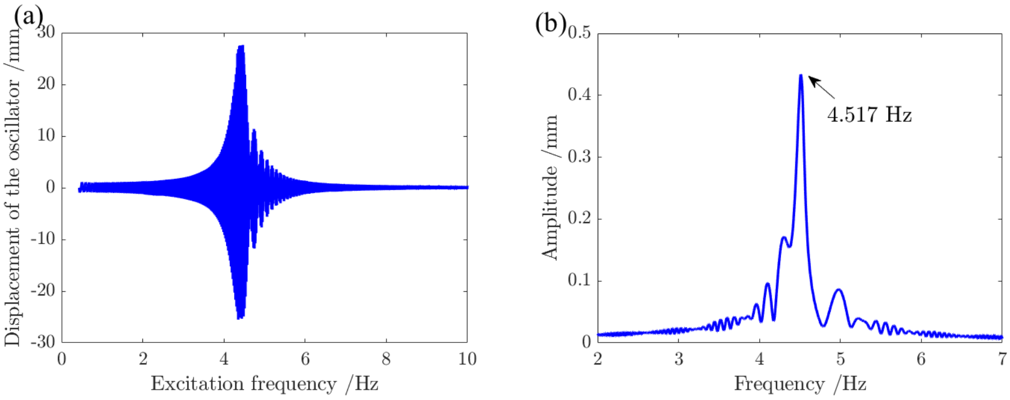

**Fig. 13** Sweep excitation results of the host structure: (a) Displacement of the endpoint; (b) Spectrum analysis.

The restoring force surface (RFS) method is a graphical tool that can effectively detect and visualize nonlinear systems, and has been used in the system identification of NES [64, 82-89]. According to Newton's second law, discrete nonlinear systems have the following characteristics,

$$m_n\ddot{w} - F_e = F_n(w, \dot{w}). \tag{26}$$

where $F_e$ is the externally applied force can be expressed as $F_e = -m_n\ddot{u}$, and $F_n(\dot{w}\ \ddot{w})$ is the restoring force of the MTNES, containing the damping force and nonlinear restoring force provided by the coupling of spring and magnets. The idea of RFS is to use measurements where $\dot{w}$ is small to fit a stiffness force, and measurements where $w$ is small to fit a damping force. To verify the accuracy of the restoring force model of the MTNES calculated by Eq. (1) and to obtain the equivalent viscous damping coefficient $c_n$ of the MTNES, it is necessary to obtain $w$, $\dot{w}$, $\ddot{w}$, $\ddot{u}$, and $F_e$. A stepped sine motion with a frequency from 0.5 Hz to 5 Hz is applied to the cantilever beam to acquire the acceleration ($\ddot{w}$) of the oscillator and the displacement ($u$) at the endpoint of the cantilever beam.

Fig. 14 (a) shows the stiffness curve calculated via Eq.(1) and measured data of the MTNES. The blue dots are the data obtained from the experiment and the red curve is the expected stiffness force of the MTNES, calculated from Eq. (1). The points for $\dot{w}$ range from -0.01 m/s to 0.01 m/s are picked. These points are close to the MTNES restoring force curve, which proves that Eq. (1) can effectively predict the nonlinear stiffness restoring force of the device. The points for $w$ range from -0.0005 m to 0.0005 m are chosen to plot Fig. 14(b). Linear fitting is performed on these points, and the obtained viscous damping coefficient $c_n$ of MTNES is 4.83 N·s/m and will be used in the following numerical analysis.

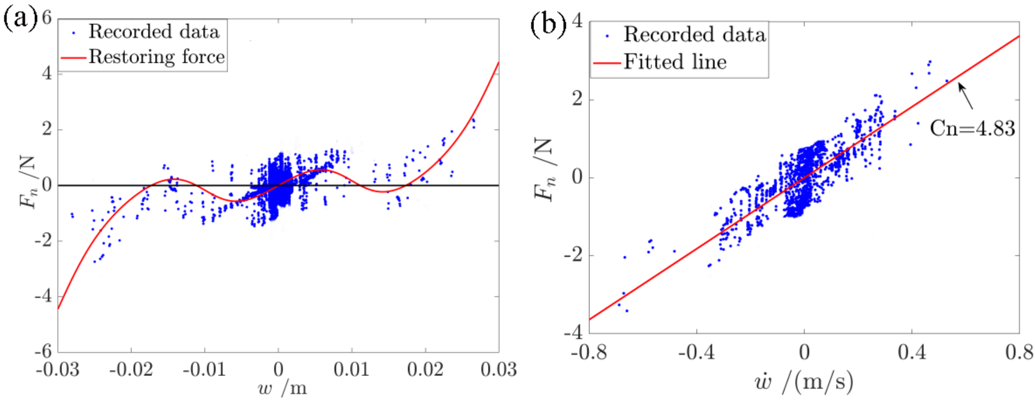

**Fig. 14** Restoring force curve and measured data: (a) Stiffness force; (b) Damping force.

## 5.3 Vibration damping performance and discussion

The experimental performance of the NES is now investigated. The excitation is a cosine sweep signal with a frequency range from 0.5 Hz to 10 Hz. The amplitudes of the external loads are 60 N and 150 N, respectively. The displacement of the endpoint of the cantilever beam with and without MTNES is shown in Fig .15.

It is evident that when the excitation frequency of the external load is below 3.4 Hz, the MTNES cannot effectively control the vibration of the cantilever beam because the energy in the host system fails to reach the threshold required to activate the MTNES. When the frequency of the external load is from 3.4 Hz to 5 Hz, the MTNES can effectively suppress the vibration of the cantilever beam and reduce the displacement response of the cantilever beam. When subjected to frequency sweep excitation with an external load of 60 N, the maximum displacement response at the endpoint decreases from 0.018 m (without MTNES) to 0.011 m (with MTNES). Similarly, the maximum response at the endpoint of the cantilever beam decreases from

0.028 m (without MTNES) to 0.013 m (with MTNES) when the external excitation load is 150 N.

With an external load of 60 N, the oscillator moves between stable point 1 and stable point 3 due to the low energy input from the external load. However, for the external force is 150 N, when the load frequency is between 3.8 Hz and 4.5 Hz, the oscillator continuously undergoes steady-state transitions and target energy transfer, as shown in Fig. 16.

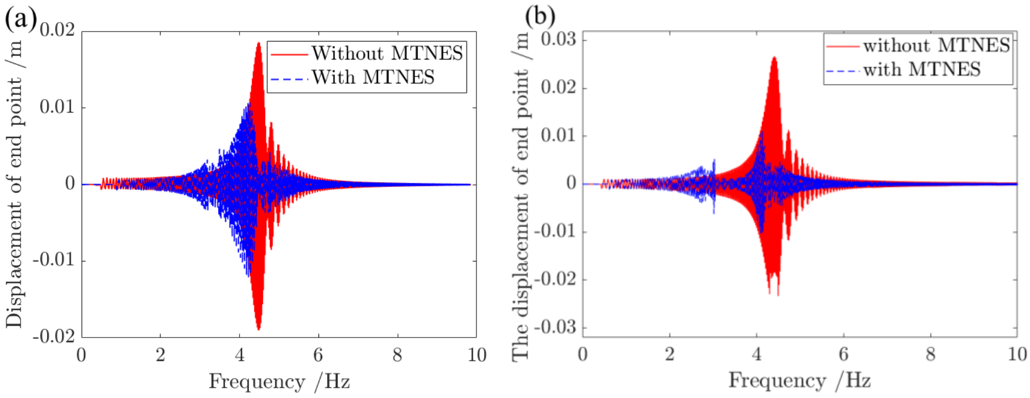

**Fig.15** The displacement of endpoint under sweep frequency excitation: (a) $F$=60 N; (b) $F$=150 N.

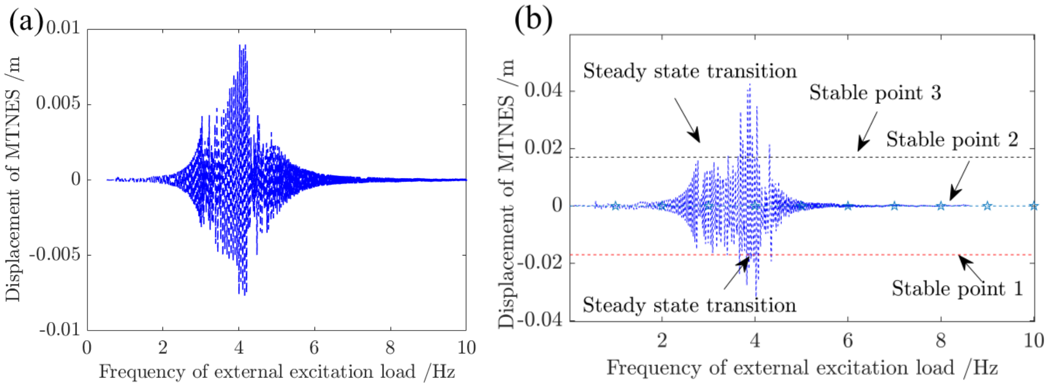

**Fig.16** The relative displacement of the oscillator under sweep frequency excitation: (a) $F$=60 N; (b) $F$=150 N.

The excitation is altered to a fixed signal with frequencies ranging from 3.7 Hz to 5.0 Hz, and each excitation period lasts for 60 seconds. Fig.17 displays the displacement response of the endpoint of the cantilever beam with and without MTNES under different fixed frequency excitations (3.8 Hz, 4.4 Hz, and 5.0 Hz) when the external force is 150 N. These figures depict both the displacement response obtained from the experiment (Fig. 17(a), Fig. 17(c), Fig. 17(e)) and the RK method (Fig. 17(b), Fig. 17(d), Fig. 17(f)). As illustrated in Fig. 17(a) and Fig. 17(b), when the excitation frequency of the external force is 3.8 Hz ($\overline{\Omega} = 0.84$), both the cantilever beams with and without MTNES show steady-state excitation responses and the MTNES begins to exhibit vibration suppression effect.

When the external load excitation frequency is 4.4 Hz ($\overline{\Omega} = 0.98$), the so-called strongly modulated response (SMR) occurs, where the vibrations of both the host structure (as shown in Fig.17(c) and Fig. 17(d)) and the MTNES modulate (as shown in Fig.18). In this case, the displacement response of the host structure with control has the characteristics of maximum and minimum values. The displacement response of the endpoint of the uncontrolled system reaches 0.053 m, while the RMS of the coupled structure is only 0.018 m, the displacement suppression efficiency reaches up to 66%.

When the external load excitation frequency reaches 5.0 Hz ($\overline{\Omega}$ = 1.11), as displayed in Fig.17(e) and Fig.17(f), the displacement responses of both the controlled and uncontrolled structures tend to be steady-state responses, again. It means that the MTNES has a wide vibration absorption frequency band near the resonance frequency of the host structure. For an external load of 60 N, the responses of endpoint with and without MTNES are both steady-state responses, which will not be explained any more, The specific experimental results will be described in Fig. 19.

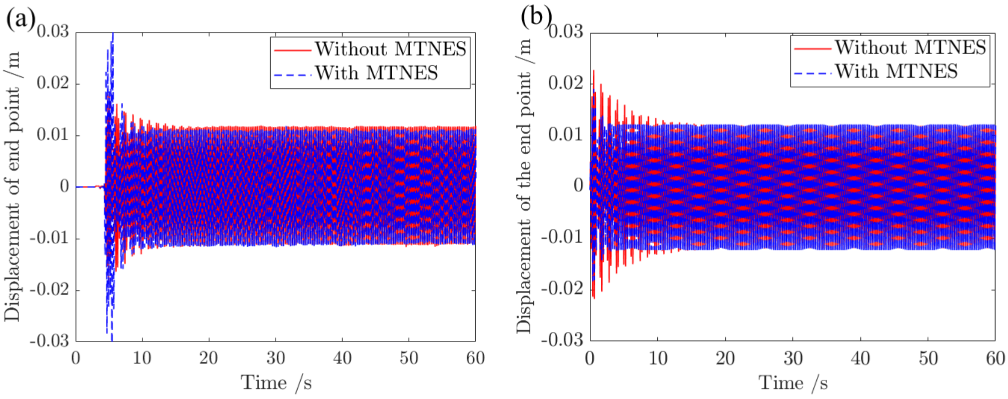

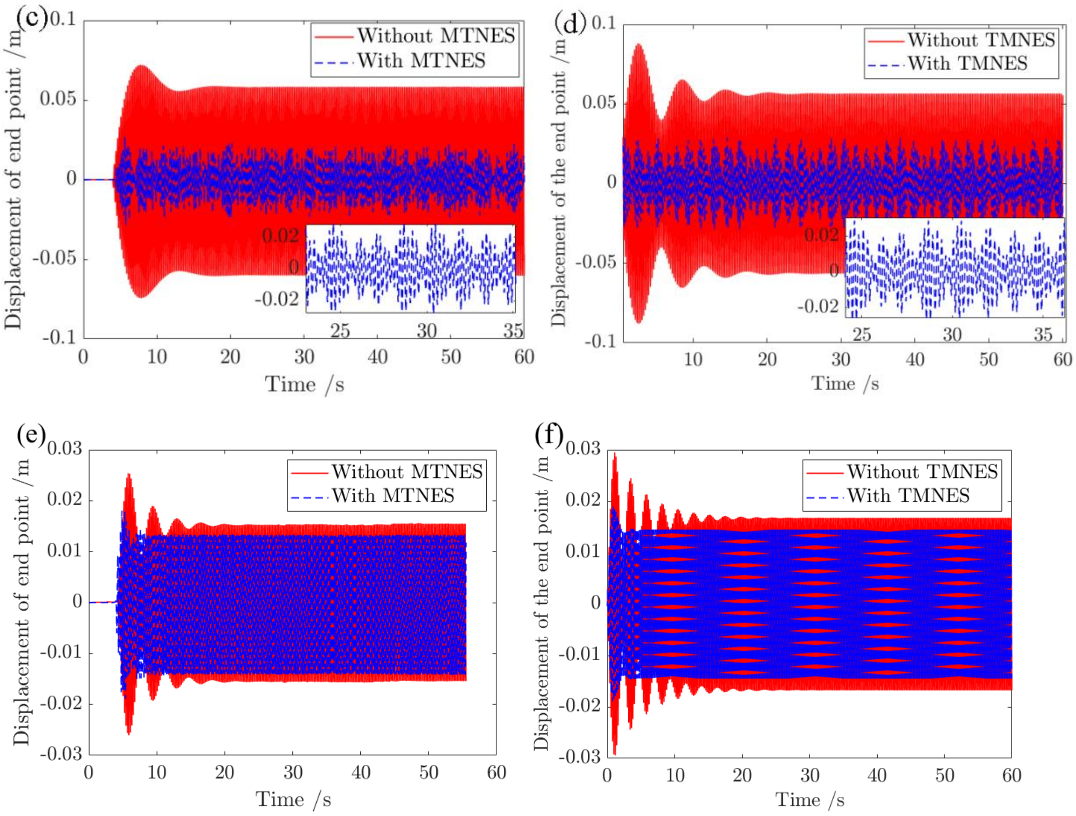

**Fig.17** The displacement response of the endpoint under different external load frequency excitation (with and without MTNES): (a) 3.8 Hz (experiment); (b) 3.8 Hz (RK method); (c) 4.4 Hz (experiment); (d) 4.4 Hz (experiment); (e) 5.0 Hz (experiment); (f) 5.0 Hz (RK method).

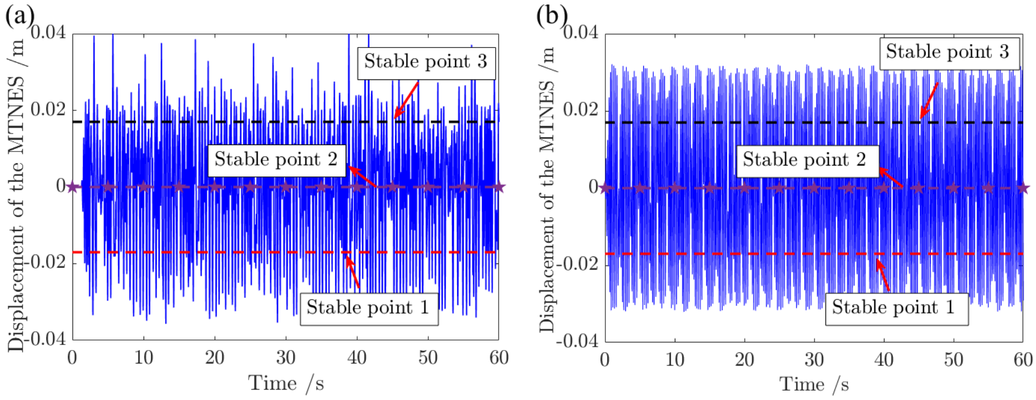

**Fig.18** The displacement response of the oscillator when the excitation frequency is 4.4 Hz: (a) Experiment; and (b) RK method.

Fig. 19 compares the displacement response from the RK method, the experiment, and the HB method under various frequency excitations. No matter whether the external force is 60 N and 150 N, the evolving trends of the three sets of data demonstrate consistency, indicating the effectiveness of the simplified MTNES restoring force model in predicting the response of the coupled structure.

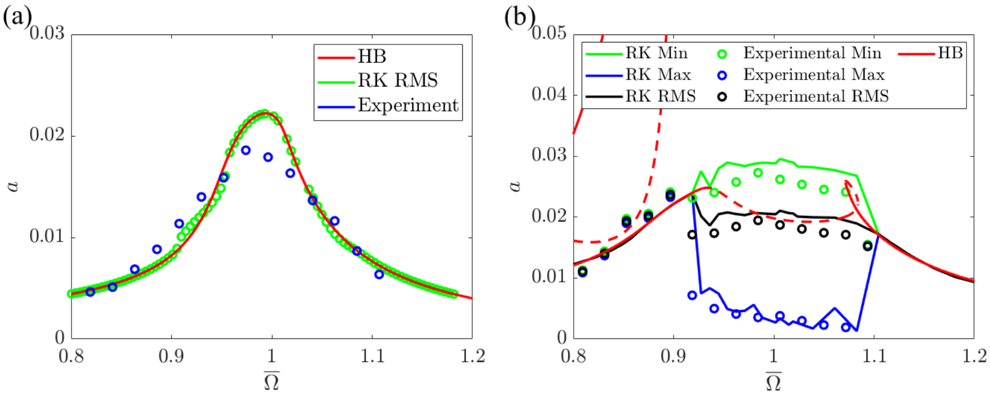

**Fig.19** Comparison of the displacement response among the RK method, the experiment, and the HB method: (a) $F$=60 N; (b) $F$=150 N.

## 6. Conclusion

To address the limited performance of traditional tuned mass damper, which only exhibits effective vibration suppression near the resonance frequency of the host structure and has a narrow vibration suppression band, this research introduces a magnetic tri-stable nonlinear energy sink (MTNES) by combining a linear spring and magnets to get the nonlinear restoring force. The proposed MTNES is applied to alleviate bending vibration in a cantilever beam and the following conclusions are drawn.

(1). Through the reasonable selection of the magnets, stiffness of the spring, and arrangement of these elements, the proposed MTNES can effectively create a vibration-absorbing device featuring three symmetrical stable characteristic points. The global optimization method is used to calculate the objective function, which includes the energy dissipation term and the displacement suppression term when the coupled structure is subjected to impact loads, to obtain the parameters of the MTNES system. An important point is, this method is not only for cantilever beams, but for any system coupled with NES.

(2). The polynomial form is used to fit the elastic-magnetic coupling restoring force in MTNES, which can well describe the motion characteristics of the coupled system within the limited motion range of the oscillator. The harmonic balance method and the Runge-Kutta method are used to calculate the displacement response of the coupled system, and the obtained system displacement responses exhibit remarkable consistency. Additionally, it is verified that MTNES can suppress the vibration of the cantilever beam in a wide frequency band.

(3). According to the experimental results, it can be found that the proposed MTNES for suppressing the bending vibration of the cantilever beam is effective, significantly reducing the amplitude of the host structure near the resonance frequency by 66%. Moreover, the restoring force method is used to identify the parameters of the MTNES. The experimental and simulation results are in good agreement for the amplitude of harmonic excitation load of 60N and 150N. The research offers a novel approach for mitigating vibrations of beam structures or rod structures, presenting a new device for further exploration in vibration control.

## Appendix A. Stability criterion of SIM

Linearizing the second equation of Eq. (22) at the fixed point $B_{eq} = B - \Delta_B$ obtained from the solutions of Eq. (23), the stability of the solutions on the SIM is described as,

$$\begin{bmatrix} \dot{\Delta}_B \\ \dot{\Delta}_B^* \end{bmatrix} = \underbrace{\begin{bmatrix} a_{11} & a_{12} \\ a_{21} & a_{22} \end{bmatrix}}_{\Theta} \begin{bmatrix} \Delta_B \\ \Delta_B^* \end{bmatrix}. \tag{A-1}$$

where $\Delta_B = B - B_{eq}$ and

$$\begin{aligned} a_{11} &= a^*{}_{22} = -iX - \xi_n \sqrt{X} + \sum_{\gamma=1}^{9} \frac{\gamma+1}{2} k_\gamma C_\gamma^{\frac{\gamma+1}{2}} B^{\frac{\gamma-1}{2}} B^{*\frac{\gamma-1}{2}} \Bigg|_{B=B_{eq}} \quad (\gamma = 1,3,5,7,9), \\ a_{12} &= a^*{}_{21} = i \sum_{\gamma=1}^{9} \frac{\gamma-1}{2} k_\gamma C_\gamma^{\frac{\gamma-1}{2}} B^{\frac{\gamma+1}{2}} B^{*\frac{\gamma-3}{2}} \Bigg|_{B=B_{eq}} \quad (\gamma = 1,3,5,7,9). \end{aligned} \tag{A-2}$$

The eigenvalues of the Jacobian matrix $\Theta$ dictate the stability. Positive real eigenvalues indicate instability of the fixed point.

## Appendix B. Stability criterion under harmonic load

The calculation of the stability for the harmonic balanced Eq. (21) involves assessing the linear stability around the equilibrium points *A* and *B*, where $\Delta_A = A - A_{eq}$, $\Delta_B = B - B_{eq}$ and

$$i2\sqrt{X} \begin{bmatrix} \dot{\Delta}_A \\ \dot{\Delta}_A^* \\ \dot{\Delta}_B \\ \dot{\Delta}_B^* \end{bmatrix} = \underbrace{\begin{bmatrix} a_{11} & a_{12} & a_{13} & a_{14} \\ a_{21} & a_{22} & a_{23} & a_{24} \\ a_{31} & a_{32} & a_{33} & a_{34} \\ a_{41} & a_{42} & a_{43} & a_{44} \end{bmatrix}}_{\Psi} \begin{bmatrix} \Delta_A \\ \Delta_A^* \\ \Delta_B \\ \Delta_B^* \end{bmatrix}, \tag{B-1}$$

$$a_{12} = a_{21} = a_{32} = a_{41} = 0, \tag{B-2}$$

$$a_{11} = -a^*{}_{22} = -\varepsilon\sigma - i\varepsilon\xi\sqrt{X}, \tag{B-3}$$

$$a_{13} = -a_{24}^* = i\varepsilon\xi_n\sqrt{X} + \varepsilon \sum_{\gamma=1}^{9} \overline{k_\gamma} \frac{\gamma+1}{2} C_\gamma^{\frac{\gamma+1}{2}} B^{\frac{\gamma-1}{2}} B^{*\frac{\gamma-1}{2}} \Bigg|_{B=B_{eq}} \quad (\gamma = 1,3,5,7,9), \tag{B-4}$$

$$a_{14} = -a_{23}^* = \varepsilon \sum_{\gamma=1}^{9} \overline{k_\gamma} \frac{\gamma-1}{2} C_\gamma^{\frac{\gamma+1}{2}} B^{\frac{\gamma+1}{2}} B^{*\frac{\gamma-3}{2}} \Bigg|_{B=B_{eq}} \quad (\gamma = 1,3,5,7,9), \tag{B-5}$$

$$a_{31} = -a_{42}^* = 1 + i\varepsilon\xi\sqrt{X}, \tag{B-6}$$

$$a_{33} = -a_{44}^* = X - \frac{1+\varepsilon}{\varepsilon} a_{13}, \tag{B-7}$$

$$a_{34} = -a_{43}^{*} = -\frac{1+\varepsilon}{\varepsilon} a_{14}. \tag{B-8}$$

If any eigenvalue of matrix Ψ possesses a real part greater than zero, the point is deemed unstable.

## Acknowledgment

The authors gratefully acknowledge the National Natural Science Foundation of China (Grant No.51878151), National Natural Science Foundation of China (Grant No.12102100), China Scholarship Council (No.202206090067), and a post-doc fellowship of the Special Research Fund (BOF) from the Flemish Government awarded by Ghent University (BOF22/PDO/022). At the same time, we would like to thank all the reviewers who provided constructive comments on this article for their hard work.

### Data availability statements

The datasets analyzed during the current study are available from the corresponding author on reasonable request.

### Declarations

**Conflict of interest** The authors declare no conflict of interest in preparing this article. The datasets generated during and/or analyzed during the current study are available from the corresponding author on reasonable request.

**Human and animal rights** No human or animal subjects were used in this work.

# References:

[1] Elias, S., Matsagar, V.: Research developments in vibration control of structures using passive tuned mass dampers. Annu Rev Control. **44**, 129-156 (2017). https://doi.org/10.1016/j.arcontrol.2017.09.015

[2] Soto, M.G, Adeli, H.: Tuned mass dampers. Arch Comput Method E. **20**(4), 419-431 (2013). https://doi.org/10.1007/s11831-013-9091-7

[3] Pinkaew, T., Lukkunaprasit, P., Chatupote, P.: Seismic effectiveness of tuned mass dampers for damage reduction of structures. Eng Struct. **25**(1), 39-46 (2003). https://doi.org/10.1016/S0141-0296(02)00115-3

[4] Rahimi, F., Aghayari, R., Samali, B.: Application of tuned mass dampers for structural vibration control: A state-of-the-art review. Civil Engineering Journal-Tehran. **6**(8), 1622-1651 (2020). https://doi.org/10.28991/cej-2020-03091571

[5] Ding, H., Chen, L.Q.: Design, analysis, and applications of nonlinear energy sinks. Nonlinear Dynam. **100**(04), 3061-3107 (2020). https://doi.org/10.1007/s11071-020-05724-1

[6] Lu, Z., Wang, Z.X., Zhou, Y., Lv, X.L.: Nonlinear dissipative devices in structural vibration control: A review. J Sound Vib. **423**, 18-49 (2018). https://doi.org/10.1016/j.jsv.2018.02.052

[7] Gendelman, O.V., Manevitch, L.I., Vakakis, A.F., M'Closkey, R.: Energy pumping in nonlinear mechanical oscillators: Part I - Dynamics of the underlying Hamiltonian systems. J Appl Mech - T ASME. **68**(1), 34-41 (2001). https://doi.org/10.1115/1.1345524

[8] Vakakis, A.F., Gendelman, O.V.: Energy pumping in nonlinear mechanical oscillators: Part II - resonance capture. J Appl Mech-T ASME. **68**(1), 42-48. (2001) https://doi.org/10.1115/1.1345525

[9] Manevitch, L.I., Musienko, A.I., Lamarque, C.H.: New analytical approach to energy pumping problem in strongly nonhomogeneous 2dof systems. Meccanica. **42**(1), 77-83 (2007). https://doi.org/10.1007/s11012-006-9021-y

[10] Kerschen, G., Peeters, M., Golinval, J.C., Vakakis, A.F.: Nonlinear normal modes, Part I: A useful framework for the structural dynamicist. Mech Syst Signal Pr. **23**(1), 170-194 (2009). https://doi.org/10.1016/j.ymssp.2008.04.002

[11] Peeters, M., Viguié, R., Sérandour, G., Kerschen, G., Golinval, J.C.: Nonlinear normal modes,

Part II: Toward a practical computation using numerical continuation techniques. Mech Syst Signal Pr. **23**(1), 195-216 (2009). https://doi.org/10.1016/j.ymssp.2008.04.003

[12] Al-Shudeifat, M.A.: Highly efficient nonlinear energy sink. Nonlinear Dynam. **76**(4), 1905-1920 (2014). https://doi.org/10.1007/s11071-014-1256-x

[13] Manevitch, L.I., Sigalov, G., Romeo, F., Bergman, L.A., Vakakis, A.: Dynamics of a linear oscillator coupled to a bistable light attachment: Analytical study. J Appl Mech-T ASME. **81**(4), 041011 (2014). https://doi.org/10.1115/1.4025150

[14] Romeo, F., Sigalov, G., Bergman, L.A., Vakakis, A.F.: Dynamics of a linear oscillator coupled to a bistable light attachment: Numerical study. J Comput Nonlin Dyn. **10**(1),011007 (2015). https://doi.org/10.1115/1.4025150

[15] Romeo, F., Manevitch, L.I., Bergman, L.A., Vakakis, A.: Transient and chaotic low-energy transfers in a system with bistable nonlinearity. Chaos. **25**(5), 53109 (2015). https://doi.org/10.1063/1.4921193

[16] Fang, X., Wen, J.H., Yin, J.F., Yu, D.L.: Highly efficient continuous bistable nonlinear energy sink composed of a cantilever beam with partial constrained layer damping. Nonlinear Dynam. **87**(4), 2677-2695 (2017). https://doi.org/10.1007/s11071-016-3220-4

[17] Habib ,G., Romeo, F.: The tuned bistable nonlinear energy sink. Nonlinear Dynam. **89**(1): 179-196 (2017). https://doi.org/10.1007/s11071-017-3444-y

[18] Dekemele, K., Van Torre, P., Loccufier, M.: Performance and tuning of a chaotic bi-stable NES to mitigate transient vibrations. Nonlinear Dynam. **98**(3), 1831-1851 (2019). https://doi.org/10.1007/s11071-019-05291-0

[19] Yao, H.L., Wang, Y., Xie, L., Wen, B.: Bi-stable buckled beam nonlinear energy sink applied to rotor system. Mech Syst Signal Pr. **138**, 106546 (2020). https://doi.org/10.1016/j.ymssp.2019.106546

[20] Chen, Y.Y., Qian, Z.C., Zhao, W., Chang, C.M.: A magnetic bi-stable nonlinear energy sink for structural seismic control. J Sound Vib. **473**, 115233 (2020). https://doi.org/10.1016/j.jsv.2020.115233

[21] Chen, Y.Y., Su, W.T., Tesfamariam, S., Qian, Z.C., Zhao, W., Shen, C.Y., Zhou, F.L.:

Experimental testing and system identification of the sliding bistable nonlinear energy sink implemented to a four-story structure model subjected to earthquake excitation. Journal of Building Engineering. **61**, 105226 (2022). https://doi.org/10.1016/j.jobe.2022.105226

[22] Chen, Y.Y., Su, W.T., Tesfamariam, S., Qian, Z.C., Zhao, W., Yang, Z.Y., Zhou, F.L.: Experimental study of magnetic bistable nonlinear energy sink for structural seismic control. Soil Dyn Earthq Eng. **164**, 107572 (2023). https://doi.org/10.1016/j.soildyn.2022.107572

[23] Chen, L., Liao, X., Xia, G.F., Sun, B.B., Zhou, Y.: Variable-potential bistable nonlinear energy sink for enhanced vibration suppression and energy harvesting. Int J Mech Sci. **242**,107997 (2023). https://doi.org/10.1016/j.ijmecsci.2022.107997

[24] Fang, S.T., Chen, K.Y., Xing, J.T., Zhou, S.X., Liao, W.H.: Tuned bistable nonlinear energy sink for simultaneously improved vibration suppression and energy harvesting. Int J Mech Sci. **212**,106838 (2021). https://doi.org/10.1016/j.ijmecsci.2021.106838

[25] Lvm X.L., Liu, Z.P., Lu, Z.: Optimization design and experimental verification of track nonlinear energy sink for vibration control under seismic excitation. Struct Control Heal Monit **24**(12), e2033 (2017). https://doi.org/10.1002/stc.2033

[26] Wang, J.J., Wierschem, N.E., Spencer, B.F., Lu, X.L.: Track nonlinear energy sink for rapid response reduction in building structures. J Een Mech. **141**(1), 1-10 (2015) https://doi.org/10.1061/(ASCE)EM.1943-7889.0000824

[27] Wang, J.J., Wierschem, N.E., Spencer, B.F., Lu, X.L.: Experimental study of track nonlinear energy sinks for dynamic response reduction. Eng Struct. **94**, 9-15 (2015). https://doi.org/10.1016/j.engstruct.2015.03.007

[28] Wang, J.J., Wierschem, N.E., Wang, B., Spencer, B.F.: Multi-objective design and performance investigation of a high-rise building with track nonlinear energy sinks. Struct Design Tall Spec Build. **29**(02), e1692 (2020). https://doi.org/10.1002/tal.1692

[29] Dou, J.X., Yao, H.L., Li, H., Li, J.L., Jia, R.Y.: A track nonlinear energy sink with restricted motion for rotor systems. Int J Mech Sci. **259**, 108631 (2023). https://doi.org/10.1016/j.ijmecsci.2023.108631

[30] Nucera, F., Vakakis, A.F., Mcfarland, D.M., Bergman, L.A., Kerschen, G.: Targeted energy

transfers in vibro-impact oscillators for seismic mitigation. Nonlinear Dynam. **50**(3), 651-677 (2007). https://doi.org/10.1007/s11071-006-9189-7

[31] Nucera, F., Lacono, F.L., McFarland, D.M., Bergman, L.A., Vakakis, A.F.: Application of broadband nonlinear targeted energy transfers for seismic mitigation of a shear frame: Experimental results. J Sound Vib. **313**(1-2), 57-76 (2008). https://doi.org/10.1016/j.jsv.2010.01.020

[32] Nucera, F., McFarland, D.M., Bergman. L.A., Vakakis, A.F.: Application of broadband nonlinear targeted energy transfers for seismic mitigation of a shear frame: Computational results. J Sound Vib. **329**(15), 2973-2994 (2010). https://doi.org/10.1016/j.jsv.2010.01.020

[33] Li, T., Seguy, S., Berlioz, A.: Dynamics of cubic and vibro-impact nonlinear energy sink (NES): analytical, numerical, and experimental analysis. J Vib Acoust. **138**(3), 031010 (2016). https://doi.org/10.1115/1.4032725

[34] Ahmadi, M., Attari, N.K.A., Shahrouzi, M.: Structural seismic response mitigation using optimized vibro-impact nonlinear energy sinks. J Earthq Eng. **19**(2), 193-219 (2014). https://doi.org/10.1080/13632469.2014.962671

[35] Li, H.Q., Li, A., Zhang, Y.F.: Importance of gravity and friction on the targeted energy transfer of vibro-impact nonlinear energy sink. Int J Impact Eng. **157**, 104001 (2021). https://doi.org/10.1016/j.ijimpeng.2021.104001

[36] Rong, K.J., Yang, M., Lu, Z., Zhang, J.W., Tian, L., Wu, S.Y.: Energy analysis of a nonlinear gas-spring dynamic vibration absorber subjected to seismic excitations. Journal of Building Engineering. **89,** 109253 (2024). https://doi.org/10.1016/j.jobe.2024.109253

[37] Rong, K.J., Lu, Z., Zhang, J.W., Zhou, M.Y., Huang, W.Y.: Nonlinear gas-spring DVA for seismic response control: Experiment and numerical simulation. Eng Sturct. **283**, 115940 (2023). https://doi.org/10.1016/j.engstruct.2023.115940

[38] Qiu, D.H., Seguy, S., Paredes, M.: Tuned nonlinear energy sink with conical spring: design theory and sensitivity analysis. J Mech Design. **140**(1), 011404 (2018). https://doi.org/10.1115/1.4038304

[39] Rong, K.J., Lu, Z.: A novel nonlinear gas-spring TMD for the seismic vibration control of a MDOF structure. Struct Eng Mech. **83**(1), 31-43 (2022).

https://doi.org/10.12989/sem.2022.83.1.031

[40] Yao, H.L., Cao, Y.B., Ding, Z.Y., Wen, B.C.: Using grounded nonlinear energy sinks to suppress lateral vibration in rotor systems. Mech System Signal Pr. **124**, 237-253 (2019). https://doi.org/10.1016/j.ymssp.2019.01.054

[41] Sigalov, G., Gendelman, O.V., Al-Shudeifat, M.A., Manevitch, L.I., Vakakis, A.F., Bergman, L.A.: Resonance captures and targeted energy transfers in an inertially-coupled rotational nonlinear energy sink. Nonlinear Dyn. **69**(4), 1693-1704 (2012). https://doi.org/10.1007/s11071-012-0379-1

[42] Kong, X.R., Li, H.Q., Wu, C.: Dynamics of 1-dof and 2-dof energy sink with geometrically nonlinear damping: application to vibration suppression. Nonlinear Dyn. **91**(1), 733-754 (2018). https://doi.org/10.1007/s11071-021-06615-9

[43] Silva, T.M.P., Clementino, M.A., Erturk, A., De Marqui, C.: Equivalent electrical circuit framework for nonlinear and high quality factor piezoelectric structures. Mechatronics. **54**, 133-143 (2018). https://doi.org/10.1016/j.mechatronics.2018.07.009

[44] Silva, T.M.P., Clementino, M.A., De Marqui, C., Erturk, A.: An experimentally validated piezoelectric nonlinear energy sink for wideband vibration attenuation. J. Sound Vib. **437**, 68-78 (2018). https://doi.org/10.1016/j.jsv.2018.08.038Get rights and content

[45] Raze G, Kerschen G. Multimodal vibration damping of nonlinear structures using multiple nonlinear absorbers. Int J Non-Linear Mech. **119**, 103308 (2020). https://doi.org/10.1016/j.ijnonlinmec.2019.103308

[46] Wierschem, N.E., Quinn, D.D., Hubbard, S.A., Al-Shudeifat, M.A., McFarland, D.M., Luo, J., Fahnestock, L.A., Spencer, B.F., Vakakis, A.F., Bergman, L.A. Passive damping enhancement of a two-degree-of-freedom system through a strongly nonlinear two-degree-of-freedom attachment. J Sound Vib. **331**(25), 5393-5407 (2012). https://doi.org/10.1016/j.jsv.2012.06.023

[47] Taghipour, J., Dardel, M.: Steady state dynamics and robustness of a harmonically excited essentially nonlinear oscillator coupled with a two-DOF nonlinear energy sink. Mech Syst Signal Pr. **62-63**,164-182 (2015). https://doi.org/10.1016/j.ymssp.2015.03.018

[48] Zhou, S., Lallart, M., Erturk, A.: Multistable vibration energy harvesters: Principle, progress, and perspectives. J Sound Vib. **528**, 116886 (2022). https://doi.org/10.1016/j.jsv.2022.116886

[49] Liu, C.R., Liao, B.P., Zhao, R., Yu, K.P., Pueh Lee, H., Zhao, J.: Large stroke tri-stable vibration energy harvester: Modelling and experimental validation. Mech Syst Signal Pr. **168,** 108699 (2022). https://doi.org/10.1016/j.ymssp.2021.108699

[50] Schmidt, F., Lamarque, C.H.: Energy pumping for mechanical systems involving non-smooth Saint-Venant terms. Int J Nonlin Mech. **45**(9): 866-875. (2010) https://doi.org/10.1016/j.ijnonlinmec.2009.11.018

[51] Lamarque, C.H., Savadkoohi, A.T.: Targeted energy transfer between a system with a set of saint-venant elements and a nonlinear energy sink. Continuum Mech Therm. **27**(4), 819-833 (2015). https://doi.org/10.1007/s00161-014-0354-9

[52] Al-Shudeifat, M.A.: Asymmetric magnet-based nonlinear energy sink. J Comput Nonlin Dyn. **210**(1), 01450 (2015). https://doi.org/10.1115/1.4027462

[53] Fang, X., Wen, J.H., Yin, J.F., Yu, D.L.: Highly efficient continuous bistable nonlinear energy sink composed of a cantilever beam with partial constrained layer damping. Nonlinear Dynam. **87**(4), 2677-2695 (2017). https://doi.org/10.1007/s11071-016-3220-4

[54] Saeed, A.S., Al-Shudeifat, M.A., Vakakis, A.F.: Rotary-oscillatory nonlinear energy sink of robust performance. Int J Nonlin Mech. **117**, 103249 (2019). https://doi.org/10.1016/j.ijnonlinmec.2019.103249

[55] Chen, Y.Y., Qian, Z.C., Zhao, W., Chang, C.M.: A magnetic Bi-stable nonlinear energy sink for structural seismic control. J Sound Vib. **473**, 115233 (2020). https://doi.org/10.1016/j.jsv.2020.115233

[56] Zeng, Y.C., Ding, H.: A tristable nonlinear energy sink. Int J Mech Sci. **238**, 107839 (2023). https://doi.org/10.1016/j.ijmecsci.2022.10783

[57] Rezaei, M., Talebitooti, R., Liao, W.H.: Exploiting bi-stable magneto-piezoelastic absorber for simultaneous energy harvesting and vibration mitigation. Int J Mech Sci. **207**, 106618 (2021). https://doi.org/10.1016/j.ijmecsci.2021.106618

[58] Rezaei, M., Talebitooti, R., Liao, W.H.: Concurrent energy harvesting and vibration suppression utilizing PZT-based dynamic vibration absorber. Arch Appl Mech. **92**(1), 363-82 (2022). https://doi.org/10.1007/s00419-021-02063-4

[59] Rezaei, M., Talebitooti, R.: Investigating the performance of tri-stable magnetopiezoelastic absorber in simultaneous energy harvesting and vibration isolation. Appl Math Model. **102**, 661-693 (2022). https://doi.org/10.1016/j.apm.2021.09.044

[60] Lo Feudo, S., Touze, C., Boisson, J., Cumunel, G.: Nonlinear magnetic vibration absorber for passive control of a multi-storey structure. J Sound Vib. **438**, 33-53 (2019). https://doi.org/10.1016/j.jsv.2018.09.007

[61] Yao, H.L.,Cao, Y.B., Wang, Y.W., Wen, B.C.: A tri-stable nonlinear energy sink with piecewise stiffness. J Sound Vib. **463**, 114971 (2019). https://doi.org/10.1016/j.jsv.2019.114971

[62] Yao, H.L., Wang, Y.W., Cao, Y.B., Wen, B.C.: Multi-stable nonlinear energy sink for rotor system. Int J Nonlin Mech. **118**, 103273 (2020). https://doi.org/10.1016/j.ijnonlinmec.2019.103273

[63] Wang, Y.W., Yao, H.L., Han, J.C., Li, Z.A., Wen, B.C.: Application of non-smooth NES in vibration suppression of rotor-blade systems. Appl Math Model. **87**, 351-371 (2020). https://doi.org/10.1016/j.apm.2020.06.014

[64] Fu, J.D., Wan, S., Zhou, P., Shen, J.W., Loccufier, M., Dekemele, K.: Effect of magnetic-spring bi-stable nonlinear energy sink on vibration and damage reduction of concrete double-column piers: Experimental and numerical analysis. Eng Struct. **303**, 117517 (2024). https://doi.org/10.1016/j.engstruct.2024.1175

[65] Wu, W.J., Chen, X.D., Shan, Y.H.: Analysis and experiment of a vibration isolator using a novel magnetic spring with negative stiffness. J Vib Control. **333**(13), 2958-2970 (2014). https://doi.org/10.1016/j.jsv.2014.02.009

[66] Allag, H., Yonnet, J.P.: 3-D analytical calculation of the torque and force exerted between two cuboidal magnets. IEEE Trans Magn. **45**, 3969-3972 (2009). https://doi.org/10.1109/TMAG.2009.2025047

[67] Yang, Y.Q., Wang, X.: Investigation into the linear velocity response of cantilever beam embedded with impact damper. J Vib Control. **25**(7), 1-14 (2019). https://doi.org/10.1177/107754631882171

[68] Li, W.K., Wierschem, N.E., Li, X.H., Yang, T.J., Brennan, M.J.: Numerical study of a symmetric single-sided vibro-impact nonlinear energy sink for rapid response reduction of a

cantilever beam. Nonlinear Dynam. **100**(2), 951-971 (2020). https://doi.org/10.1007/s11071-020-05571-0

[69] Ahmadabadi, Z.N., Khadem, S.E.: Nonlinear vibration control of a cantilever beam by a nonlinear energy sink. Mech Mach Theory. **50**, 134-149 (2012). https://doi.org/10.1016/j.mechmachtheory.2011.11.007

[70] Avramov, K.V., Gendelman, O.V.: Forced oscillations of beam with essentially nonlinear absorber. Strength Mater. **41**(3), 310-317 (2009). https://doi.org/10.1007/s11223-009-9125-4

[71] Parseh, M., Dardel, M., Ghasemi, M.H., Pashaei, M.H.: Steady state dynamics of a non-linear energy sink. Int J Nonlin Mech. **79**, 48-65 (2016). https://doi.org/10.1016/j.ijnonlinmec.2015.11.005

[72] Eurocode 1: Actions on structures - Part 2: Traffic loads on bridges. EN 1991-2 (2003).

[73] Rana, R., Soong, T.T.: Parametric study and simplified design of tuned mass dampers. Eng Struct. **20**(3), 193-204 (1998). https://doi.org/10.1016/S0141-0296(97)00078-3

[74] Rong, K.J., Lu, Z.: An improved ESM-FEM method for seismic control of particle turned mass damper on MDOF system. Appl Acoust. **172**, 107663 (2020). https://doi.org/10.1016/j.apacoust.2020.107663

[75] Zeng, Y.C., Ding, H., Ji, J.C., Jing, X.J., Chen, L.Q.: A tristable nonlinear energy sink to suppress strong excitation vibration. Mech System Signal Pr. **202**, 110694 (2023). https://doi.org/10.1016/j.ymssp.2023.110694

[76] Tian, W., Zhao, T., Yang, Z.C. Supersonic meta-plate with tunable-stiffness nonlinear oscillators for nonlinear flutter suppression. Int J Mech Sci. **229**, 107533 (2022). https://doi.org/10.1016/j.ijmecsci.2022.107533

[77] Manevitch, L.: The description of localized normal modes in a chain of nonlinear coupled oscillators using complex variables. Nonlinear Dynam. **25**, 95-109 (2001). https://doi.org/10.1023/A:1012994430793

[78] Dekemele, K.: Tailored nonlinear stiffness and geometric damping: Applied to a bistable vibration absorber. Int J Nonlin Mech. **157**, 104548 (2023). https://doi.org/10.1016/j.ijnonlinmec.2023.104548

[79] Gendelman, O.V.: Targeted energy transfer in systems with non-polynomial nonlinearity. J Vib Control. **315**(3), 732-745 (2008). https://doi.org/10.1016/j.jsv.2007.12.024

[80] Gendelman, O.V., Starosvetsky, Y., Feldman, M.: Attractors of harmonically forced linear oscillator with attached nonlinear energy sink I: Description of response regimes. Nonlinear Dyn. **51**, 31-46 (2008). https://doi.org/10.1007/s11071-006-9167-0

[81] Gendelman, O.V.: Bifurcations of nonlinear normal modes of linear oscillator with strongly nonlinear damped attachment. Nonlinear Dynam. **37**(2), 115-128 (2004). https://doi.org/10.1023/B:NODY.0000042911.49430.25

[82] Wu, T.M., Huang, J.L., Zhu, W.D.: Quasi-periodic oscillation characteristics of a nonlinear energy sink system under harmonic excitation. J Sound Vib. **572**, 118143 (2024). https://doi.org/10.1016/j.jsv.2023.118143

[83] Wang, Y.F., Kang, H.J., Cong, Y.Y., Guo, T.D., Zhu, W.D.: Vibration suppression of a cable under harmonic excitation by a nonlinear energy sink. Commun Nonlinear SCI. **117**, 106988 (2023). https://doi.org/10.1016/j.cnsns.2022.106988

[84] Wang, X., Geng, X.F., Mao, X.Y., Ding, H., Jing, X.J., Chen, L.Q.: Theoretical and experimental analysis of vibration reduction for piecewise linear system by nonlinear energy sink. Mech Syst Signal Pr. **172,** 109001 (2022). https://doi.org/10.1016/j.ymssp.2022.109001

[85] Luo, J., Wierschem, N.E., Hubbard, S.A., Fahnestock, L.A., Quinn, D.D., McFarland, D.M., Spencer, B.F., Vakakis, A.F., Bergman, L.A.: Large-scale experimental evaluation and numerical simulation of a system of nonlinear energy sinks for seismic mitigation. Eng Struct. **77**, 34-48 (2014). https://doi.org/10.1016/j.engstruct.2014.07.020

[86] Masri, S., Caughey, T.: A nonparametric identification technique for nonlinear dynamic problems. J Appl Mech. **46**(2), 433-477 (1979). https://doi.org/10.1115/1.3424568

[87] Dekemele, K., Van Torre, P., Loccufie,r M.: Design,construction and experimental performance of a nonlinear energy sink in mitigating multi-modal vibrations. J Sound Vib. **473**, 115243 (2020). https://doi.org/10.1016/j.jsv.2020.115243

[88] Kerschen, G., Worden, K., Vakakis, A.F., Golinval, J.C.: Past, present and future of nonlinear system identification in structural dynamics. Mech Syst Signal Pr. **20**(3), 505-592 (2005).

https://doi.org/10.1016/j.ymssp.2005.04.008

[89] Noël, J., Kerschen, G.: Nonlinear system identification in structural dynamics: 10 more years of progress. Mech Syst Signal Pr. **83**, 2-35 (2017). https://doi.org/10.1016/j.ymssp.2016.07.020